

# IMPERIAL COLLEGE LONDON

## FINAL REPORT FOR MENG PROJECT

---

### **Cybathlon 2020 Powered Exoskeleton Race**

---

**Closing the sensory and control loop of assistive gait technology for spinal cord injury patients - a center of pressure estimation with vibrotactile feedback case study**

---

**Author:**

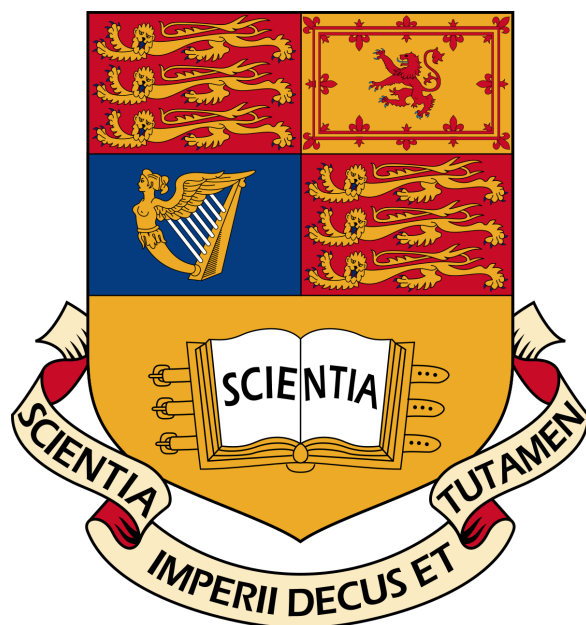
Charalambos Hadjipanayi

**CID:**

01077219

**Supervisor:** Professor Dario Farina

Submitted in partial fulfilment of the requirements for the award of MEng in Biomedical Engineering from Imperial College London



## Abstract

Powered lower-limb exoskeletons provide motion assistance to spinal cord injury (SCI) patients by replacing or restoring their lost and independent locomotion ability; thus, allowing patients to safely perform daily activities and improve their life quality. Recent research is emphasized on exoskeleton control methods that can recognize and predict the user's motion intention with different signals as motion indicators. This study proposes an external portable system that can potentially enhance the performance of a myoelectrically-controlled lower-limb exoskeleton for SCI patients. The developed feedback platform can provide – through the use of a foot-sole pressure detection system – additional feedback signals to the exoskeleton controller, based on foot plantar pressure distributions captured during gait. The gait dynamics captured by the foot pressure sensing system can also be used as input sensory signals to a haptic system located in user's upper body, to encourage closed-loop control of the exoskeleton. The foot pressure sensing prototype system developed in this project consists of an array of six force-sensitive elements embedded in a shoe-insole, that can capture plantar pressure variations with a Root of Sum Squared (RSS) error value of 3.4478% and resolution 4.7998 kPa. The proposed haptic feedback system has the capability to map foot plantar pressure signals into three levels of vibrotactile stimulation on user's index finger, with overall classification accuracy of 84.2% under noisy experimental conditions obtained from psychometric tests based on haptic perception.

## Acknowledgements

I would like to express my gratitude to all people who were supporting me during my MEng Project. To begin with, I am tremendously grateful to my supervisor, Professor Dario Farina, chairman of the Neurorehabilitation Lab at Imperial College London, for the opportunity to conduct this study, work within his research group and for all the invaluable guidance and advice from his expertise in the field. Secondly, I would like to say a massive thank you to Dr Deren Yusuf Barsakcioglu and Dr Hsien-Yung Huang for supporting me constantly with the project, being always there to assist with any matter, providing me with useful solutions to project-related issues and making the project a pleasure to work on. Specifically, I would like to thank Deren for all his assistance in electronic aspects of the project as well helping me with project allocation process. I also sincerely thank Hsien-Yung for providing me with information about mechanical aspects of project, helping me with silicone moulding procedure and supplying me with numerous literature resources.

Additionally, I am also thankful for all the help and advice on circuit design for Foot Pressure Sensing System and Haptic Feedback System from Mr Paschal Egan. The compression tests would not have been possible without the massive assistance of Mr Niraj Kanabar. Furthermore, I would like to extend my gratitude to all people working in Professor Farina's group for creating a very friendly environment to work in and being always willing to help. Finally, I am most grateful to Department of Bioengineering at Imperial College London for funding the project.

# Contents

<b>Contents</b>	<b>ii</b>
<b>1 Introduction</b>	<b>1</b>
<b>2 Foot Pressure Sensing System</b>	<b>3</b>
2.1 Methods . . . . .	3
2.1.1 System Design . . . . .	3
2.1.2 Force Sensor Calibration . . . . .	5
2.1.3 Silicone Mould Creation . . . . .	6
2.1.4 Sampling Rate of Foot Pressure Sensing system . . . . .	7
2.1.5 Complete System Assembly . . . . .	7
2.2 Results . . . . .	9
2.3 Discussion . . . . .	11
<b>3 Haptic Feedback System</b>	<b>12</b>
3.1 Methods . . . . .	12
3.1.1 System Design . . . . .	12
3.1.2 Evaluation of Amplitude Modality and Stimulation Waveform . . . . .	14
3.1.3 Evaluation of Position Modality . . . . .	16
3.2 Results . . . . .	18
3.3 Discussion . . . . .	20
<b>4 Conclusion</b>	<b>21</b>
<b>5 Bibliography</b>	<b>22</b>
<b>6 Appendices</b>	<b>27</b>
6.1 Center of Pressure Calculations . . . . .	27
6.2 Alignment and resampling steps for FPS system . . . . .	28
6.3 Sensor Properties calculations . . . . .	30
6.4 Silicone Mould Preparation details . . . . .	31
6.5 Polynomial Regression models for each trial . . . . .	33
6.6 Average Polynomial Regression models . . . . .	36
6.7 Silicone mould effects on Force-Voltage models . . . . .	39
6.8 Waveform Description for Amplitude Modality . . . . .	40
6.9 Details on Position-Modality Circuit . . . . .	41
6.10 Confusion Matrices . . . . .	42
6.10.1 Analysis of Confusion Matrices from perceptual experiments . . . . .	42
6.10.2 Normalisation of Confusion Matrices . . . . .	43
6.10.3 Mathematical Definitions . . . . .	44
6.10.4 Per-class Performance metrics of all methods . . . . .	45

# Chapter 1

## Introduction

Spinal cord injuries (SCI), frequently caused by trauma or disease, result in complete or partial loss of patients' motor function and are estimated to affect 250,000-500,000 patients globally every year according to World Health Organisation [1]. Daily tasks such as mobility are considered challenging or even impossible for SCI patients with leg paraplegia without reliance on walking aids or carers. Hence, significant amount of research has been dedicated on lower-limb exoskeletons [2]. This technology is essential for providing gait assistance [3] and allowing restoration of patient's independent locomotion ability through rehabilitation [4].

The vast majority of studies on powered lower-limb exoskeletons aimed at new control strategies for enhancements of their performance and human-exoskeleton interaction. Some studies focused primarily on manual controllers, such as pushbutton/joystick [5] or voice commands [6], using pre-defined gait trajectories of exoskeleton. Other studies, have utilised high-level control strategies based on user's motion intention providing greater conformity between the exoskeleton and patient motion. Different model-based control methods have been proposed utilising different motion-indicator signals, including centre of gravity (CoG) shift and upper body orientation variations [7], compressive force magnitudes in crutches [8] and infrared sensor signals [9]. Bioelectrical signals were also used in several studies, including electroencephalography (EEG) [10] or electromyography (EMG) signals.

EMG-driven control models have been applied for control of upper-limb exoskeletons [11], and lower-limb exoskeletons for hemiplegia patients [12] and paraplegia (SCI) patients [13]. In the lower-limb exoskeleton studies, the EMG signals were obtained only from lower extremity muscles, such as flexor/extensor muscles of hip and knee. In the research conducted by Jansen O. et al, a combination of EMG and weight shift signals of SCI patient, were used as inputs to the neurologically-controlled HAL Exoskeleton [14].

A novel, motion-intention based, myoelectric control method has been proposed by Professor Farina's research group, for motion control of a Trunk-Hip-Knee powered exoskeleton (Exo-H3, Technaid [15]). This lower-limb exoskeleton will then be used by complete thoracic or lumbar spinal cord injured (SCI) pilots in 2020 Cybathlon competition [16]. The proposed algorithm can potentially allow intention-based walking support to SCI patients, enabling them to perform activities of daily life, e.g. sitting down and standing up, walking, and stair ascending/descending. In this method, surface Electromyography (sEMG) signals from upper-body (back) muscles are used as the primary input to a Multi-Layer Perceptron (MLP), to construct a regression model for predicting lower-limb joint angles during hip, knee and ankle flexion-extension [18].

Studies conducted on healthy individuals [17, 18], suggest the existence of a correlation between back muscles' activation and lower body motion. However, due to limited sEMG channels available and temporal gaps in data, it is hypothesised that the performance of the trained model is insufficient for use with SCI patients. This issue can be resolved by using additional

non-bioelectrical inputs to the MLP for model enhancement. Additionally, the non-bioelectrical information can be used for gait phase classification, for calculations of instantaneous walking speed and as a safety feature, minimising risk of accidental step initiation by exoskeleton motion controller. Moreover, the proposed sEMG-based method is an open-loop control algorithm, which does not allow the user to directly adjust errors in exoskeleton motion and can result in inaccurate and unstable exoskeleton performance. Therefore, to enhance the human-machine interaction and to introduce a closed-loop control in the system, additional sensor systems can be implemented to provide haptic feedback to the pilot.

The aim of this project is the development of an external portable system to improve the control performance of the powered lower limb exoskeleton. The developed system (Figure 1.1) provides:

1. Additional sensor information to exoskeleton motion controller based on plantar pressure measurements, specifically the centre of pressure (CoP) shift of the body, through the development of a foot pressure sensing (FPS) system.
2. Meaningful and intuitive haptic feedback to the user, based on plantar pressure measurements, through the development of a haptic feedback (HF) system.

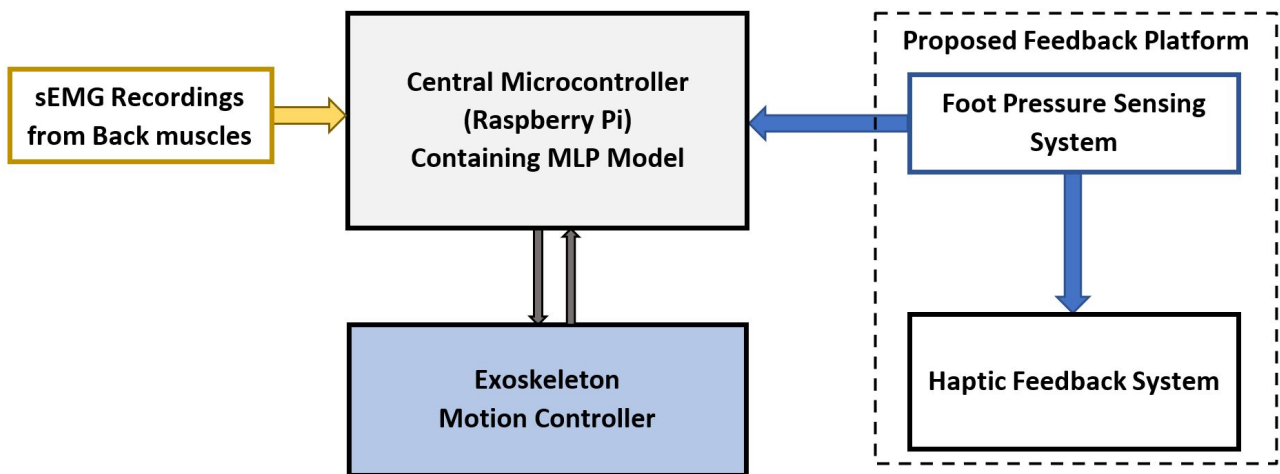


Figure 1.1: Flowchart illustrating interactions between exoskeleton motion controller and proposed feedback platform. FPS system acts as the basis of the proposed system architecture, providing feedback signals to both HF system and Central Microcontroller.

This report is organized as follows: The proposed FPS system and HF system are described in Chapters 2 and 3 respectively. Each of these chapters, is divided into sections corresponding to Methods used for design and implementation of each system, Results obtained and Discussion. In Chapter 4, a summary of the proposed systems and future improvements, is provided, followed by Bibliography and Appendices in Chapters 5 and 6.

# Chapter 2

## Foot Pressure Sensing System

Plantar pressure information is an important tool for gait cycle and posture control analysis in foot pathology diagnosis [19], sport biomechanics [20, 21], balance control improvement [22] and rehabilitation [23]. A widely used, portable method for real-time monitoring of plantar pressure distributions is the insole system, which consists of force-sensing elements embedded in the shoe insole.

Different insole monitoring system technologies have been proposed, including custom-made Velostat in-sole sensors [24, 25], Piezoresistive in-sole sensors (Flexiforce A201 (Tekscan) [26, 27] or Medical Sensor 3000E (Tekscan) [28]), and Computer Dyno Graphy systems (Infotronic) using capacitive force transducers [29]. Some of these technologies utilise high-density arrays of force-sensing elements per foot [25, 28], while others use a small set of sensors, to capture the main pressure variations in heel, metatarsal, toe and midfoot areas [26, 27]. The technologies based on sparse sets of sensors were the inspiration for the proposed system in this project, due to their lower complexity in terms of manufacturing and cost.

### 2.1 Methods

#### 2.1.1 System Design

The designed FPS system consists of two Arduino Nano (4.9mV resolution) microcontrollers (one for each leg), each powered by a 9V battery, receiving inputs from the compression load cells (force sensors) attached to the pilot's foot surface or shoe in-sole through a ribbon cable (Figure 2.1). Each microcontroller and the respective battery are enclosed in a protective box, which is attached around pilot's ankle using an elastic band.

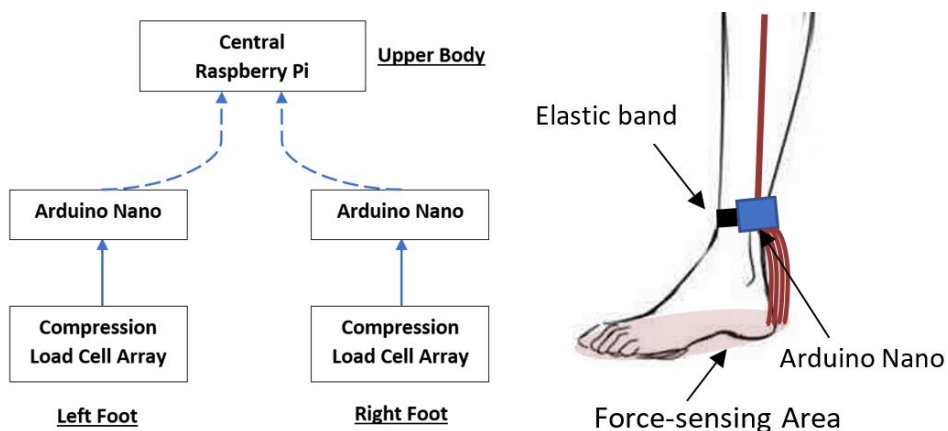


Figure 2.1: (Left) Schematic Diagram of FPS system and (Right) Location of components on the pilot's leg.

The CoP locations of each foot are computed by the responsible Arduino. The obtained values are then transmitted to the Central Microcontroller (Raspberry Pi) located in the upper body, using Inter-integrated Circuit ( $I^2C$ ) protocol, where the CoP of the whole body is calculated. This calculation requires knowledge of the instantaneous step length, stride width and pilot's lower-limb segment lengths (further details in Appendix 6.1).

The  $I^2C$  protocol was chosen over the Universal Asynchronous Receiver/Transmitter (UART) protocol to allow synchronised communication between the two Arduino boards and the Central Microcontroller. Additionally, this protocol was preferred over Serial Peripheral Interface (SPI) protocol due to long ( $\approx 1m$ ) transmission distance (ensuring less transmission errors) and its lower complexity, since there are readily available  $I^2C$  Arduino libraries.

The force sensors considered in the FPS system are force-sensitive elements which transduce vertical ground reaction forces experienced on foot surface into analogue voltage values. The relationship between input force values and voltage readings can be studied through calibration of the sensors to construct a Force-Voltage model for each sensor in the system (Section 2.1.2). After the force readings are estimated from sensor's voltage output, they are translated into pressure values through division by sensor's contact area. The FPS system operation is summarised in Figure 2.2.

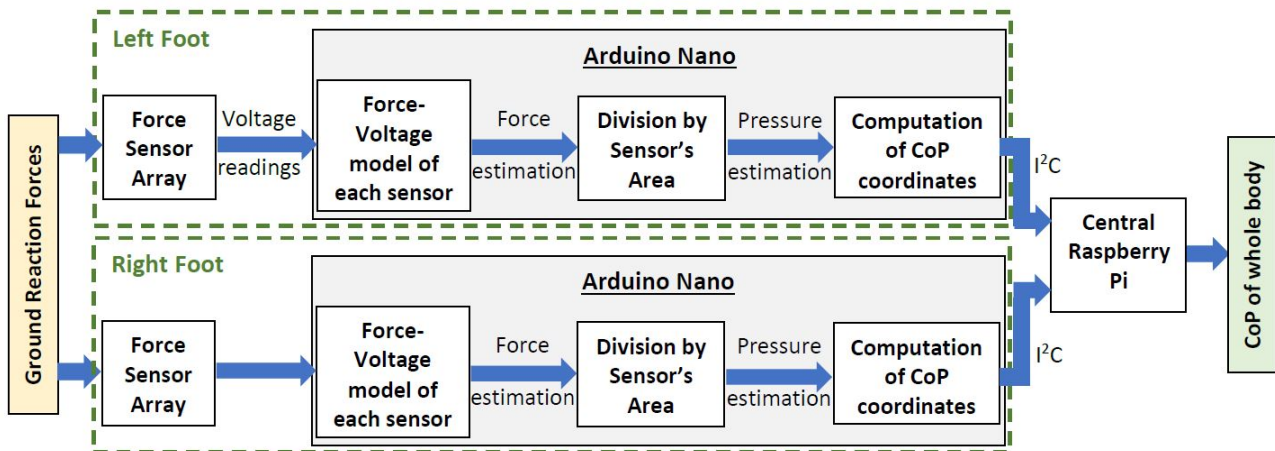


Figure 2.2: Flowchart of FPS System operation.

According to Shu et al [30], any in-sole system must ideally cover completely the 15 anatomical parts of the foot belonging to the heel, midfoot, metatarsal, and toe areas of foot sole (Figure 2.3). Based on studies conducted for analysis of plantar pressure profiles using in-Shoe systems, the maximum pressure is concentrated in the heel, metatarsal and toe areas of foot, while low pressures are also found in the midfoot area [31]. This suggests that at least three sensors are required to capture the main variations in pressure distribution that characterise gait cycle. Systems using higher number of sensors capture more accurately gait dynamics.

Each Arduino used, has six available analogue input pins for sensor connectivity (2/8 pins were used for  $I^2C$ ), thus the maximum possible number of force sensors for each leg is six. The sensor locations (Figure 2.3) are selected so that there is at least one sensor in each foot sole area. Based on [32], typical values of plantar pressures are up to 1.9MPa, however, pressures up to 3MPa have also been recorded [46]. These pressure values were taken into consideration for sensor selection.

The sensors chosen for FPS system are the TE-Connectivity FX29 series (FX293X-100A-0050-L) with 0.5-4.5V analogue output voltage and  $10^6$  full-scale cycle life. The load range is 0-50lbs (0-22.68kg) and load-sensitive area is  $13.85\text{mm}^2$ , therefore, they can successfully detect pressures up to 16.37MPa. FX29 sensors operate using DC voltage of 4.75-5.25V and have operating current of 3mA [34]. Therefore, all sensors in the array of each leg can be

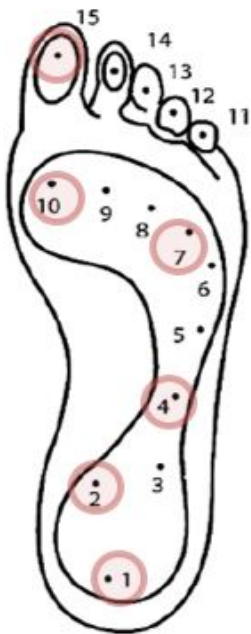


Figure 2.3: Diagram representing the 15 main foot anatomical areas that support most of the body weight and adjust the body balance. Red circles represent the selected six locations of the force sensors [30].

connected to 5V rail of Arduino, which allows a maximum output current of 400-500mA [35]. FX29 sensors offer several advantages over the FlexiForce (Table 2.1) and Velostat (pressure-sensitive conductive sheet) sensors that are widely used in literature. Based on [7, 36] Velostat-based systems have on average  $\pm 50\%$  repeatability and 24% hysteresis error, as well as low sensitivity and specificity, unless properly fabricated into specific conformations [37].

Despite these advantages, FX29 sensors have higher thickness ( $5.45 \pm 0.1\text{mm}$ ) and weight (6g) compared to FlexiForce sensors (0.203mm and 0.6g). Due to its thickness, the FX29 sensor cannot be directly mounted to foot surface but requires a mould for attachment (Section 2.1.3), which can act as a shoe in-sole. Total estimated weight of system using FX29 sensors is 250g, thus less than maximum acceptable of 300g for wearable gait sensors [39].

Table 2.1: Sensor Comparisons

	FlexiForce A201 [38]	FX29 [34]
Hysteresis Error (%)	4.5	0.8
Repeatability Error (%)	2.5	0.8
Linearity Error (%)	3	1
Thermal shift (%/ $^{\circ}\text{C}$ )	0.05	0.36

### 2.1.2 Force Sensor Calibration

A sensor validation protocol was implemented for FPS system, involving a compression test, similar to the protocol followed by [33]. A digital single-column force gauge system (MultiTest 5-xt, Mecmesin) was used and operated in compression mode. A load cell with rated capacity of 1000N was used (ILC-S 1000N) with measurement accuracy of  $\pm 0.1\%$  of full force scale (from 0-1000N) and resolution 1:6500 [40].

Before embedding sensors into a silicone mould, compression testing was initially performed on a single force sensor to allow quantification the force-voltage relationship, maximum force value and pressure range without saturation and absolute values of hysteresis and non-linearity. To study these properties, a forward and backward force sweep was performed between 0-250N at 1mm/min and the corresponding voltage readings from the Arduino were

stored using the CoolTerm software for further processing in MATLAB. To quantify the sensor properties, the force values and voltage readings required initially alignment and then resampling due to the asynchronous operation and non-equal sampling rates of MultiTest 5-xt and CoolTerm software (Appendix 6.2).

After this pre-processing step was completed, a linear regression analysis was used to find the force(F)-voltage(V) relationship in the form  $F = a_0 + a_1V$ . The regression coefficients ( $a_0, a_1$ ) were found using Least Squares method. Furthermore, the absolute values of hysteresis and non-linearity were found from Force vs Voltage plot (see Appendix 6.3).

This procedure was repeated for all sensors, to obtain an individual F-V model for each sensor. In this case, however, force sweep was performed between 0-200N to prevent sensors' output saturation. During initial tests, only six sensors corresponding to one shoe-insole were calibrated. The compression test was repeated for each of sensor over four trials and the linear force-voltage model was obtained for each trial. Performing multiple trials allowed quantification of the sensor's non-repeatability error (Appendix 6.3). The hysteresis, non-linearity and non-repeatability errors are required by International Electrotechnical Commission (IEC) 61298-2 [41] standards to quantify sensor's accuracy. To increase the expressive power of the regression models, polynomial regression was additionally implemented using the built-in MATLAB function `polyfit()`. In this method, an  $n^{\text{th}}$  order polynomial was used to describe the curvilinear relationship between the force (F) voltage (V) values in the form  $F = \sum_{i=0}^n a_i V^i$ , where the coefficients  $a_i$  were found using the Least-Squares method. This analysis was used to produce quadratic ( $n = 2$ ) and cubic ( $n = 3$ ) force-voltage models and the performance of each model was evaluated using the coefficient of determination ( $R^2$ ) and root mean-squared error (RMSE) between predicted and true force values. To obtain an average model for each sensor, the coefficients of polynomial were averaged over the four trials and the  $R^2$  and RMSE values were computed to assess performance of averaging procedure.

The calibration procedure was also repeated for a single sensor embedded in the silicone mould (Section 2.1.3) over four trials. This step was required to identify any changes in the obtained models and sensor properties due to silicone mould. Additionally, this step allowed the study of how sensor's voltage reading change as distance from sensor to contact point increases. For this test, a fixed force of 100N was applied using the force gauge system with 2cm-diameter pressure plate. To ensure reliability of results, the applied force was maintained at each location for 1min, with speed 100mm/min.

### 2.1.3 Silicone Mould Creation

A silicone mould, acting as a custom-made shoe in-sole, was prepared for force sensor attachment. The material chosen for the in-sole was the translucent SORTA-Clear™ 40 (Smooth-On) silicone rubber (readily-available in lab), with shore hardness of 40A, tensile strength of 5.52MPa (greater than maximum recorded plantar pressure [46]) and 400% elongation at break [44]. Therefore, this results in a medium-soft and flexible shoe in-sole.

For firm attachment of sensors within the in-sole, three-layer sandwich mould (Figure 2.4) was used. The sensor was embedded in Layer 2, while both Layer 1 and 3 protected the sensors and ensured that the applied pressure did not expose sensors and thus no damage could be done on pilot's feet during motion. To secure sensors and wires on Layer 1, in both the horizontal and vertical plane during Layer 2 preparation, 1mm-diameter moulding pins and silicone-based superglue (LOCSG3G, Loctite) were used. The total height of in-sole was 1.35cm, which is a typical thickness value used in in-sole studies [45]. The completed first layer of silicone mould, with a single sensor embedded, is also shown in Figure 2.4.

To prevent bubble formation, due to entrapped air, within the silicone layers, vacuum degassing was performed using KNF-N820 LABOPORT vacuum pump (further details in Appendix 6.4).

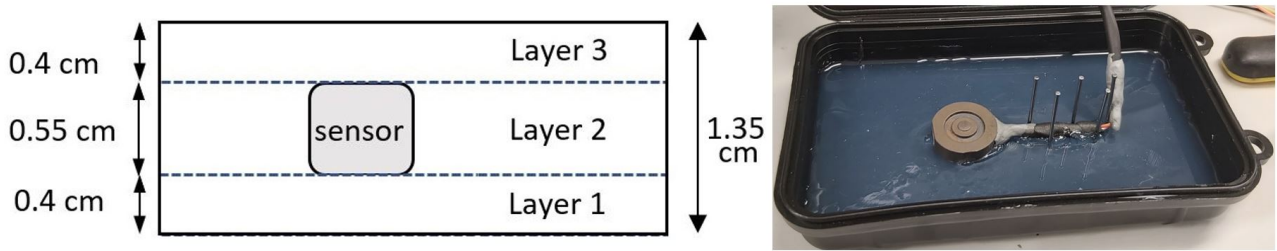


Figure 2.4: (Left) The three layers of silicone mould (side-view). (Right) Completed first layer of mould.

### 2.1.4 Sampling Rate of Foot Pressure Sensing system

An additional consideration concerning the FPS system was the sampling rate of FPS system for each leg, which according to [46], must be at least 200 Hz to capture all information concerning everyday gait tasks, without aliasing. The maximum allowable sampling rate of designed system was empirically found to be 1.18kHz. This was found by measuring, through simulations, the total time elapsed until the Central Raspberry Pi obtains CoP information. This includes time required for Arduino to read all sensor outputs, Analog-to-Digital conversion, all CoP-related computations and I<sup>2</sup>C transmission (at 100kHz), giving an average total of 850 $\mu$ s with 0.9% maximum error. To ensure lower memory requirements and a fixed regular sampling rate at 200Hz, the Arduino was commanded to start reading voltage values and perform calculations only once a pre-set time interval of 5ms has elapsed.

### 2.1.5 Complete System Assembly

Prior to embedbment of all FPS system sensors in silicone mould, sensors were connected together to allow for further system calibration/evaluation to be performed. The FX29 sensors used in this system have four wires each, with connections summarised in Table 2.2.

Table 2.2: Wire connections for FX293X-100A-0050-L sensor [34]

Wire Colour	Red	Yellow	White	Black
Connected to	V <sub>in</sub> (5V)	Analogue Pin	N/A	Ground

This means that 24 wires were needed to be connected to the Arduino for each foot. To minimise the number of wires to Arduino (for ease of troubleshooting and reduction in system complexity), common rails for power (V<sub>in</sub>) and Ground (GND) were used onto which the corresponding wires of each sensor were soldered. These rails consisted of exposed multi-core (AWG 8) wires, ensuring non-brittleness and flexibility under in-sole movements (which explains why mechanical T-connectors or star-connectors were avoided). The silicone rubber material used, insulates these rails avoiding risk of short-circuits. Additionally, a decoupling capacitor of 0.1 $\mu$ F was used between power and ground rails to reduce noise and stabilise the power supply of the circuit. Although white wires have no specific connection, they were connected to GND rail to prevent issue of cross-talking between neighbouring cables.

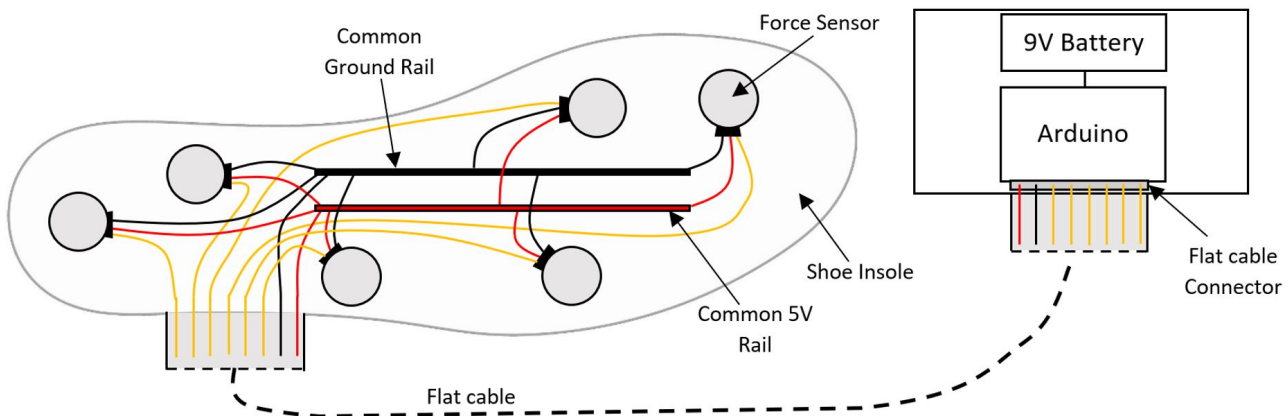


Figure 2.5: FPS system circuit diagram.

The FPS system circuit diagram is illustrated in Figure 2.5. For ease of visualisation, the white wires of each sensor were omitted. The implemented FPS system circuit is also shown in Figure 2.6, where positioning of sensors was done according to Figure 2.3.

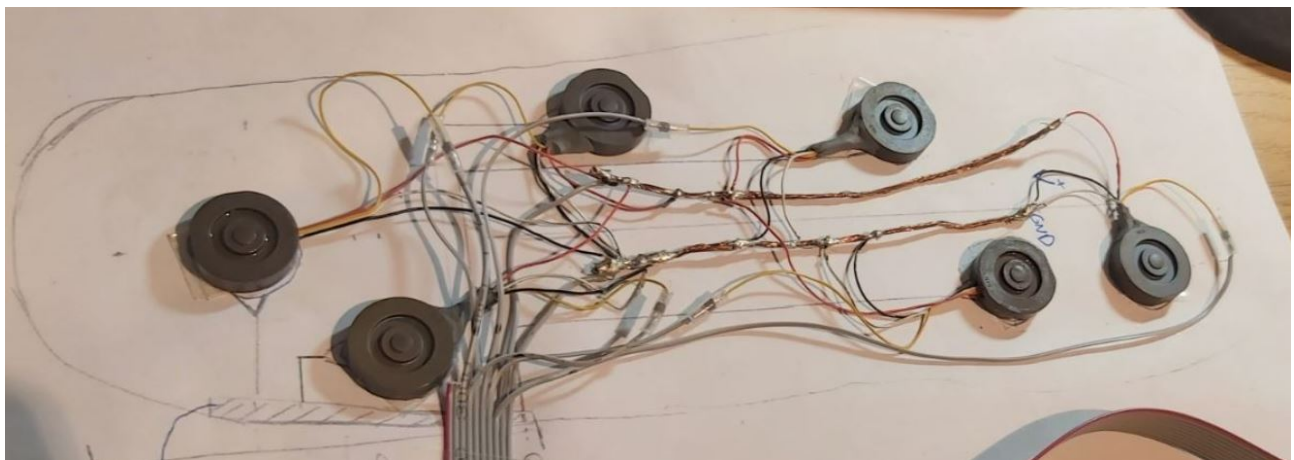


Figure 2.6: FPS system circuit implementation.

## 2.2 Results

The average linear, quadratic and cubic models for all six sensors, before embedment in silicone mould, are shown in Appendix 6.6. Based on these models, the average  $R^2$  values and RMSE values for all polynomial models of all sensors over all trials are shown in Table 2.3. Also, the polynomial models obtained in each trial for each sensor are shown in Appendix 6.5.

Table 2.3: Comparing average polynomial regression models for force estimation, before embedment in mould.

Performance Metric	Linear	Quadratic	Cubic
mean $R^2$	0.999531817	0.999533083	0.999536958
mean RMSE(N)	0.986141667	0.979266667	0.974375

Comparison done between average polynomial models for a single sensor, before and after being embedded in silicone, is shown in Appendix 6.7. The average  $R^2$  values and RMSE values of all polynomial models for all sensors over all trials are shown in Table 2.4.

Table 2.4: Comparing average polynomial regression models for force estimation, for both pre- and post-embedment in mould.

	Linear		Quadratic		Cubic	
	Pre	Post	Pre	Post	Pre	Post
mean $R^2$	0.999793	0.9982	0.999728	0.9984	0.999793	0.998475
mean RMSE(N)	0.817425	2.564475	0.81415	2.4294	0.80745	2.36665

The Force vs Voltage plot for a single sensor in one trial, before and after embedment in mould, is shown in Figure 2.7 (Enlarged plot up to 1V in Figure 2.8). The average linear model was used as best-fit line.

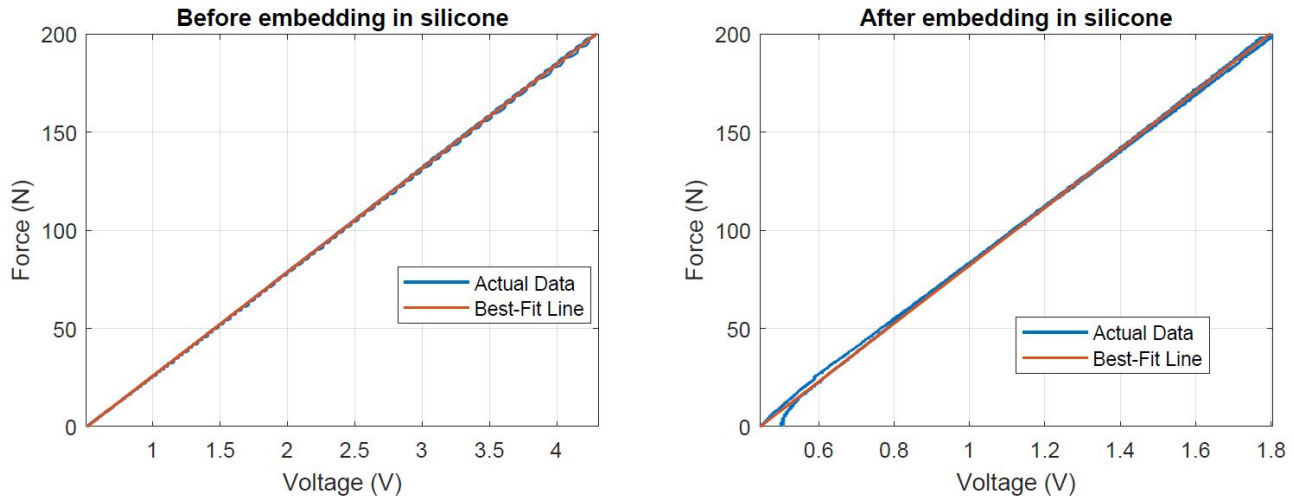


Figure 2.7: Force-Voltage plot, before and after embedding sensor in silicone mould, with estimated force values obtained from linear regression model.

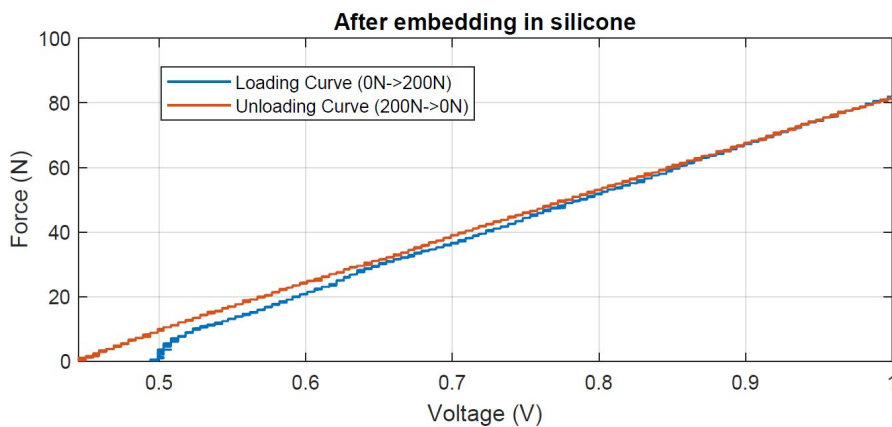


Figure 2.8: Enlarged Force-Voltage plot, after embedding sensor in silicone mould, up to 1V.

The technical characteristics of a single sensor (Serial Number:198090064), before and after being embedded in silicone mould, are compared to technical values acquired from the datasheet in Table 2.5.

Table 2.5: Empirically-obtained properties of force sensor compared to datasheet values. Value of pressure range without saturation in silicone mould, was not obtained due to lab closure (COVID-19 pandemic).

	Empirical values (not in silicone)	Empirical values (in silicone)	Datasheet values [59]
<b>Linear F-V model</b>	$F=52.9298V - 27.2803$	$F=148.117V - 65.975$	$F=56.70V - 28.15$
<b>Resolution(N)</b>	0.2585	0.723	0.2778
<b>Pressure Range without saturation (MPa)</b>	0-17.66	—	0-18.42
<b>Hysteresis absolute value (%span)</b>	0.73	1.01	0.8
<b>Non-linearity absolute value (%span)</b>	0.941	3.032	1
<b>Non-repeatability absolute value (%span)</b>	0.84	1.294	0.8
<b>Root of the Sum Squared (%)</b>	1.4574	3.4478	1.510

The graph of voltage output of same force sensor embedded in silicone mould vs distance at which a constant force of 100N is applied from sensor's center, is shown in Figure 2.9.

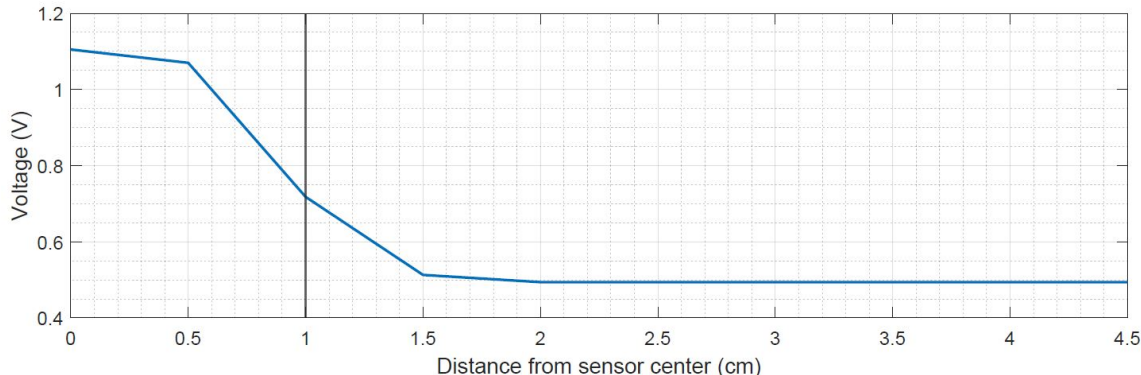


Figure 2.9: Voltage vs distance from sensor center. Vertical line denotes the radius (1cm) of pressure plate used.

## 2.3 Discussion

One important characteristic of the sensors to be used in the FPS system, is the high degree of linearity that allows accurate force predictions. The average linear models for all sensors (Table 2.3) yield high  $R^2$  (0.999532) and low RMSE values (0.98614N, i.e. 0.433% of full-span (226.796N)). Table 2.3 shows that increasing order of polynomial regression model provides insignificant increase in  $R^2$  (0.000127% and 0.000514% increase for quadratic and cubic), or decrease in RMSE values (0.00688N and 0.0118N decrease for quadratic and cubic), thus no significant improvement in expressive power of models. This is also suggested by the low linearity error obtained before embedding sensor in mould (0.941% of full-span). For this reason, the linear models for each sensor can be successfully used for force predictions, which reduces computational complexity and avoids risk of over-fitting in polynomial regression analysis.

Analysis of single-sensor calibration results, before and after being embedded in silicone mould (Table 2.4), shows that average linear models can successfully capture most of variation in force values for both cases. In post-embedment case, increasing order of polynomial (Table 2.4) does not result in significant increase of  $R^2$  (0.02% and 0.0275% increase for quadratic and cubic) or decrease of RMSE values (0.1346N and 0.1974N decrease for quadratic and cubic), thus the underlying Force-Voltage models can also be assumed linear. Moreover, an interesting phenomenon was observed in Figures 2.7-2.7 (for all trials), where in post-embedment case, the loading curve at 0N has value equal to 0.494V while unloading curve at 0N has value equal to 0.445V. To identify and analyse the source of this error (possible due to silicone-rubber properties), in future iterations of this study, sequential compression tests with cyclical force sweeps (0-200N) are required.

Apart from the Force-Voltage model differences (Table 2.5), embedding sensor in mould decreased sensor's resolution by 0.4645N, increased hysteresis error by 0.28%, non-linearity error by 2.091% (also observed by the larger magnitude of higher-order polynomial coefficients) and non-repeatability error by 0.454%. This produced a 1.9904% increase in Root of Sum Squared (RSS) value and thus a reduction in system's accuracy.

Figure 2.9 indicates that voltage value is essentially above the baseline value (0.494V) only for distances below 1.5cm from sensor's center. Since the pressure plate used was 1cm in diameter, this means that for any distance less than 1cm, the pressure plate was still in contact with sensor's sensitive area. This suggests that force readings are localised within the system, which is ideal.

Due to the COVID-19 pandemic and lab inaccessibility, further development of system was not possible. Future work includes:

1. Individual calibration of sensors, after complete system is embedded in silicone mould.
2. Analysis of sensors' output voltage using an oscilloscope, to assess the accuracy of Arduino voltage readings.
3. Comparison of complete system's performance (in CoP estimation) against commercial pedography platforms or in-sole systems, to identify prototype's non-idealities and quantify system's accuracy in capturing gait dynamics.

# Chapter 3

## Haptic Feedback System

Due to lost sensory feedback from their lower limbs, SCI patients suffer from reduced balance control, sub-optimal mobility, increased dependency on visual and auditory information and higher risks of injuries, during daily tasks. Several techniques have been proposed to provide artificial sensory feedback, based on mechanical stimulation on skin surface [47] using pneumatically-controlled [48] or motor-driven actuators [49].

Studies have shown that vibrotactile systems are limited by skin's sensory adaptation, resulting from reduced long-term perception of skin mechanoreceptors to constant mechanical stimuli [50]. Regardless of this disadvantage, vibrotactile sensors have been successful in many studies due to their simplicity for manufacture and operation.

Some studies developed haptic feedback systems to convey foot plantar pressure distributions from piezoresistive force sensors during gait, using pneumatically-controlled balloon actuators [47, 51] and piezoelectric [52] or vibrotactile actuators [53] in wearable waist or thigh bands. The technology developed in [54], translates gait events from leg angle variations (detected by inertial sensors) into motion of a skin stretch device, composed of a grooved timing belt connected to a motor. The proposed system in this report translates gait events from plantar pressure distributions on each foot into vibrotactile stimulation on upper body.

### 3.1 Methods

#### 3.1.1 System Design

The designed HF system consists of vibrotactile actuators whose activation is controlled by the Arduino on each foot, which captures the pressure distribution (Section 2.1.1).

HF systems, in general, can provide three stimulation modalities, including amplitude, position and frequency modalities, that modulate vibration waveforms based on amplitude and location of plantar pressure signals. Amplitude-modality maps pressure values into amplitudes of vibration, position-modality maps pressure values into number of motors being activated and frequency-modality maps pressure values into frequencies of vibration.

In order for pilot to successfully distinguish between modality levels, the input signal must be discretised. To achieve this, the plantar pressure values detected by the force sensors were discretised into three levels using thresholding operation (Table 3.1), based on typical values [55].

Table 3.1: Thresholds for the three tactile stimulation levels.

Stimulation Level	1	2	3	4 ('OFF')
Pressure(P) Threshold	$P \geq 230\text{kPa}$	$115\text{kPa} \leq P < 230\text{kPa}$	$19\text{kPa} \leq P < 115\text{kPa}$	$P < 19\text{kPa}$

To reduce system's complexity and produce more intuitive feedback for pilot, the six force sensors in each leg were grouped into three foot areas (Figure 3.1). Each area corresponds to one vibrotactile unit (or one vibrotactile actuator array - Section 3.1.3) on pilot's upper

body. The average pressure reading of the sensors in each area is computed by each Arduino, and the corresponding vibrotactile unit is then activated according to Table 3.1. To minimise effects of sensory adaptation, a non-constant stimulation waveform was applied, in the form of vibration bursts (pulses) or complex vibration waveforms.

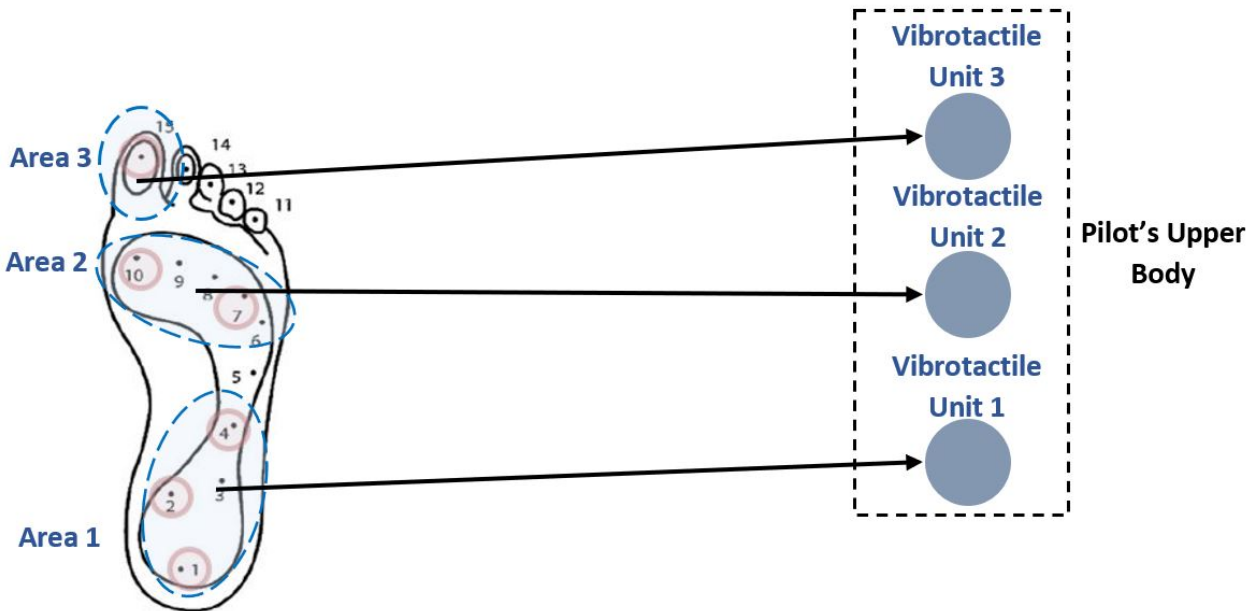


Figure 3.1: Diagram showing force sensors corresponding to each vibrotactile unit. The three areas (heel, metatarsal and toe) are the areas with highest pressure values [31].

The sensors chosen for HF system were the Adafruit 1201 vibrating mini motor discs [56], due to their compatibility with Arduino, their size (10mm diameter, 2.7mm thickness), weight (0.9g) and the widely-available documentation on their operation. Since Adafruit 1201 are eccentric rotating mass vibration motors, the amplitude of vibration is dependent on motors' angular velocity; thus, only amplitude and position modalities could be implemented. These motors can be directly connected to Arduino digital pins for ON/OFF operation. If the amplitude or shape of vibrations requires modification, then an external motor controller circuit, e.g. Adafruit DRV2605, is needed.

To evaluate the users' ability in successfully perceiving and discriminating between different haptic stimulation levels, under amplitude or position modalities, a perceptual/psychometric test was conducted for each case on 5 healthy participants, similarly to [60]. The stimulation levels used in these experiments corresponded to artificially generated pressure signals from one foot area only (one vibrotactile unit or one array used). During these experiments, participants were asked to: 1) identify minimum perceivable vibration level and 2) distinguish between different stimulation levels and patterns. For the case of amplitude modality, different stimulation waveforms were also used. The perceptual tests conducted are described in Sections 3.1.2-3.1.3.

During these experimental procedures, all vibrotactile stimulations were applied on the back-side of participant's index finger, which is known to have high concentration of vibration-sensitive Pacinian corpuscles [57, 58]. All experiments were repeated in both noisy environmental conditions, using artificially generated white noise, and noise-free conditions, where noise-cancelling ear plugs were worn by the participants. The noisy experimental conditions ensured that the effect of auditory feedback and any elements of participant's concentration were eliminated. In both conditions, the participant was asked to avoid visual contact with vibrating units. Results from noise-free experimental conditions allow identification of benchmark performance under idealised conditions, although noisy conditions resemble more closely the conditions in Cybathlon competition.

### 3.1.2 Evaluation of Amplitude Modality and Stimulation Waveform

In amplitude-modality based method of vibrotactile stimulation, the different stimulation levels represent the different vibration amplitudes of motor units. The performance of this method was evaluated in terms of classification accuracy of stimulation levels.

The experimental protocol followed, involved a training and a testing stage described below:

- Training Stage - Duration: 200s

1. The three levels of stimulation are generated sequentially by the Arduino:  
Level 1 → Level 2 → Level 3 → Level 2 → Level 1 → Level 2 → etc.
2. Two seconds delay are used between each level of stimulation.
3. Thus, each cycle of stimulation is 8s long producing a total of 25 training stage trial cycles.
4. The end of training stage is indicated by a 2s-long vibration alert.

- Testing Stage - Duration: 300s

1. The three stimulation levels are generated sequentially in a random order. Done by initializing the random number generator of Arduino, using analogRead(), on an unconnected pin.
2. Three seconds delay are used between each level of stimulation, to allow subject enough time to identify the level.
3. For a total duration of 300s, 100 random levels are generated such that accuracy in terms of a percentage is easily obtained.
4. The end of testing stage is indicated by a 2s-long vibration alert.

The aim of the training stage was to allow participants gain familiarity with the different stimulation levels and patterns. The testing stage allowed for evaluation of the amplitude-modality based method through randomly generated vibration levels. Before the training stage, the experiment protocol was briefly introduced to the participants. Subjects were asked to retain the same posture throughout the experimental procedure.

The experimental procedure described above was repeated for three different stimulation waveforms (Strong Click, Hum and Buzz), selected from the datasheet of DRV2605 controller [59], in order to identify the waveform yielding the highest accuracy (waveform description in Appendix 6.8).

For the implementation of this perceptual test, the system used (Figure 3.2) was composed of one Arduino Nano, one Adafruit 1201 vibrating motor, one Adafruit DRV2605 controller and one 1N4148 signal diode used as a fly-back diode across motor. The Arduino communicates with motor controller using I<sup>2</sup>C protocol. The implemented circuit is also shown in Figure 3.3.

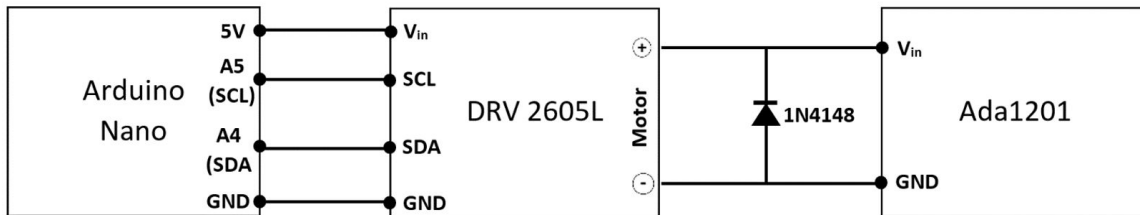


Figure 3.2: System schematic for evaluation of amplitude modality.

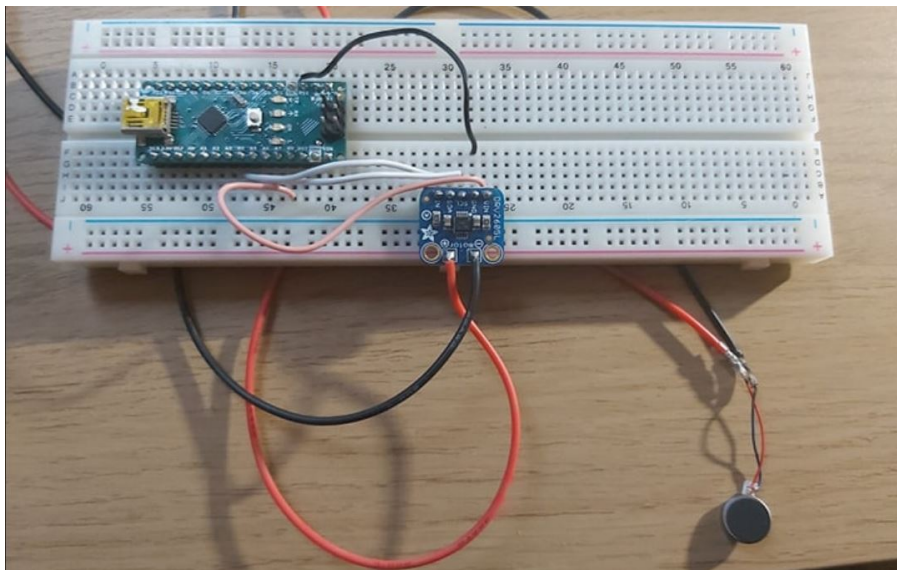


Figure 3.3: Implemented circuit used for evaluation of amplitude modality.

### 3.1.3 Evaluation of Position Modality

In position-modality based method, plantar pressure values of each foot area are mapped into an array of vibrotactile units. The different stimulation levels are represented by the number of activated motors in each motor array, placed along the back-side of index finger (Operation for one foot area shown in Figure 3.4). This can be replicated for the other two foot areas on middle finger and ring finger respectively. The experimental protocol followed for this perceptual test is identical to the protocol described in Section 3.1.2.

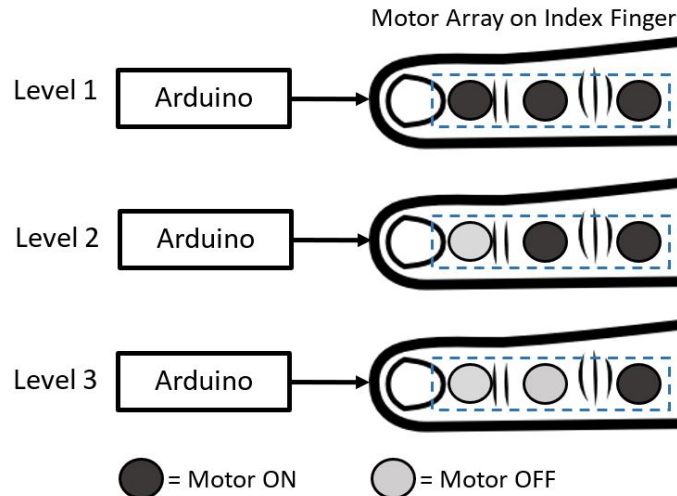


Figure 3.4: Illustration of position modality idea.

For the implementation of this test, the system used (Figure 3.5) was composed of one Arduino Nano, three Adafruit 1201 vibrating motors, three IRF520 n-Channel MOSFETs, three 1N4148 fly-back diodes, three  $220\Omega$  gate resistors (preventing ringing, i.e. parasitic oscillations) and three  $10k\Omega$  pull-down resistors (preventing capacitive or inductive coupling of MOSFETs). Each motor within the motor array is controlled by the Arduino digital pins using a low-side MOSFET switch circuit, thus motors operate in an ON/OFF mode (more details in Appendix 6.9). Each activated motor vibrates in 1s-long bursts of maximum amplitude (as rectangular pulses), separated by 2s of zero amplitude. Using 3.3V input voltage, each motor vibrates at 183Hz with 60mA current draw[59].

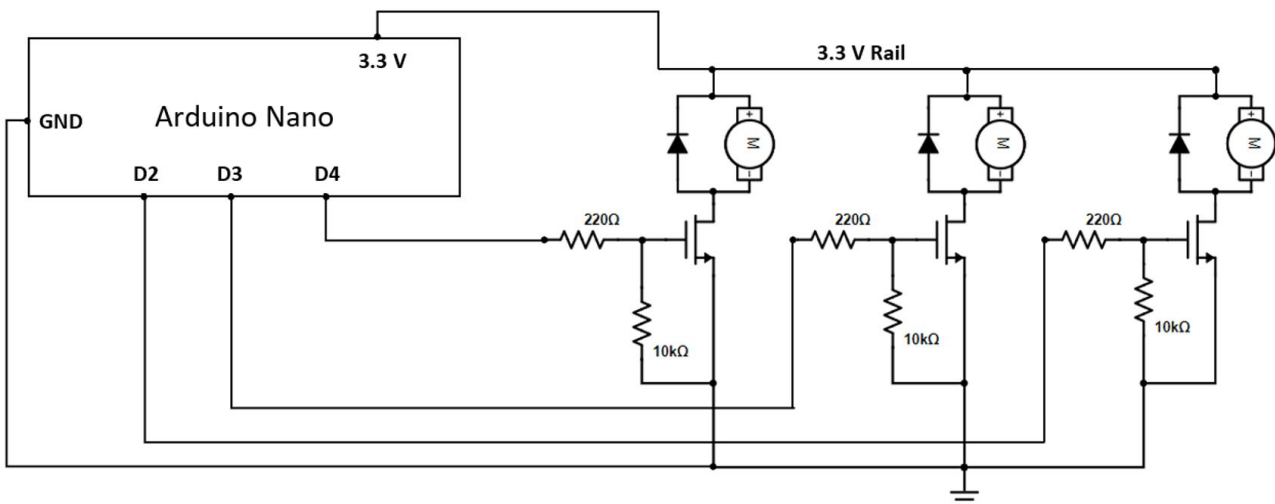


Figure 3.5: System schematic for evaluation of position modality.

The implemented circuit, after attachment of sensors to index finger, is shown in Figure 3.6. Distance between the motors on index finger was ensured to be above the two-point spatial discrimination threshold of index finger mechanoreceptors ( $> 4\text{mm}$ ) [61].

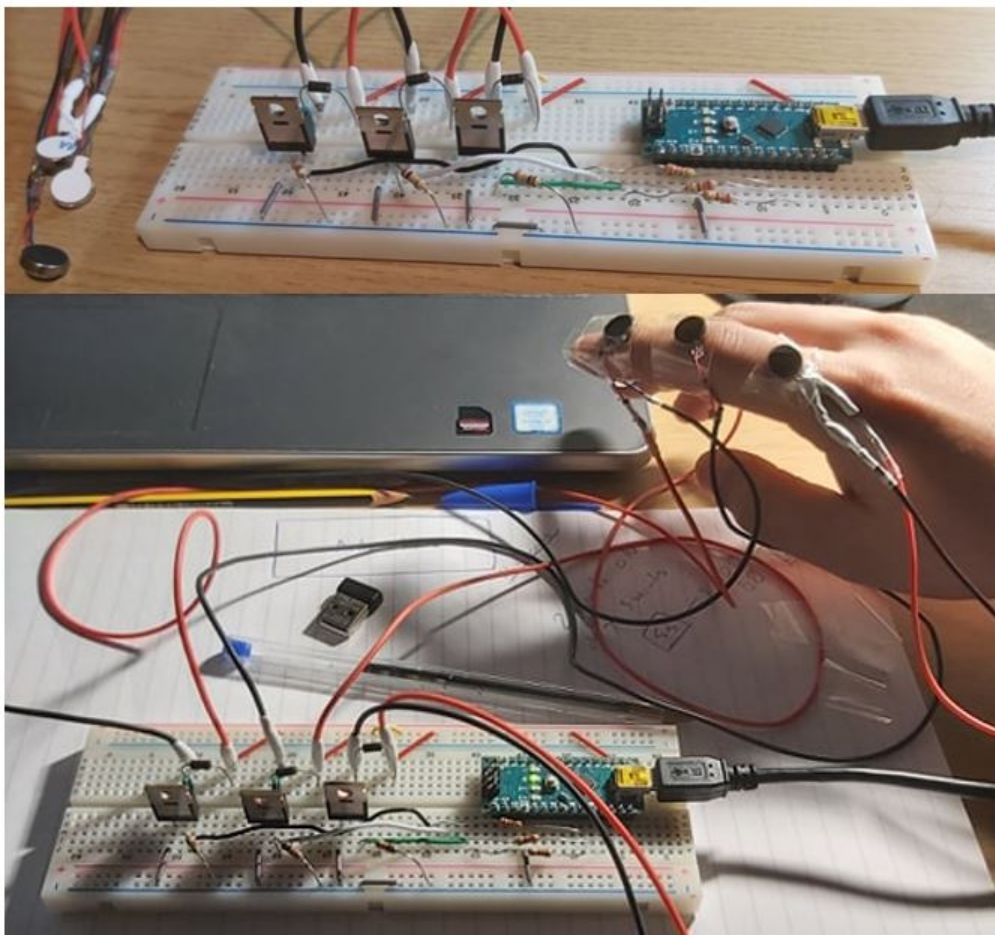


Figure 3.6: Implemented circuit for evaluation of position modality.

## 3.2 Results

Accuracy results for both amplitude and position modality are illustrated in Figure 3.7, in noise-free and noisy experimental conditions. For amplitude modality, the accuracy results of each stimulation waveform are also shown.

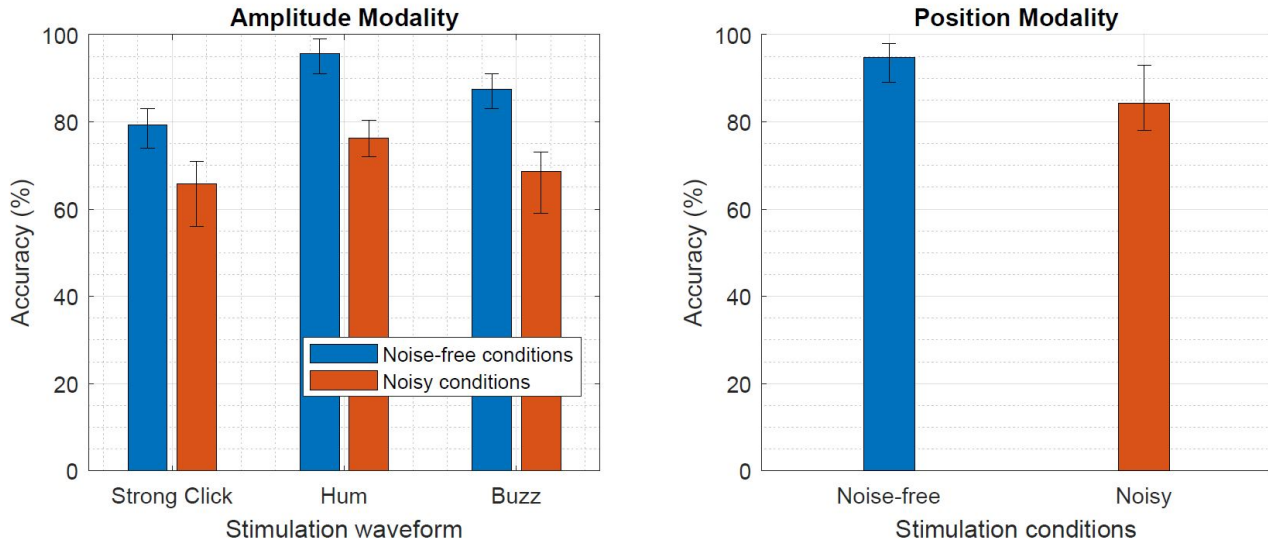


Figure 3.7: Accuracy results of amplitude and position modalities, in both noise-free and noisy experimental conditions.

The confusion matrices obtained from both perceptual experiments are shown in Figures 3.8 and 3.9.

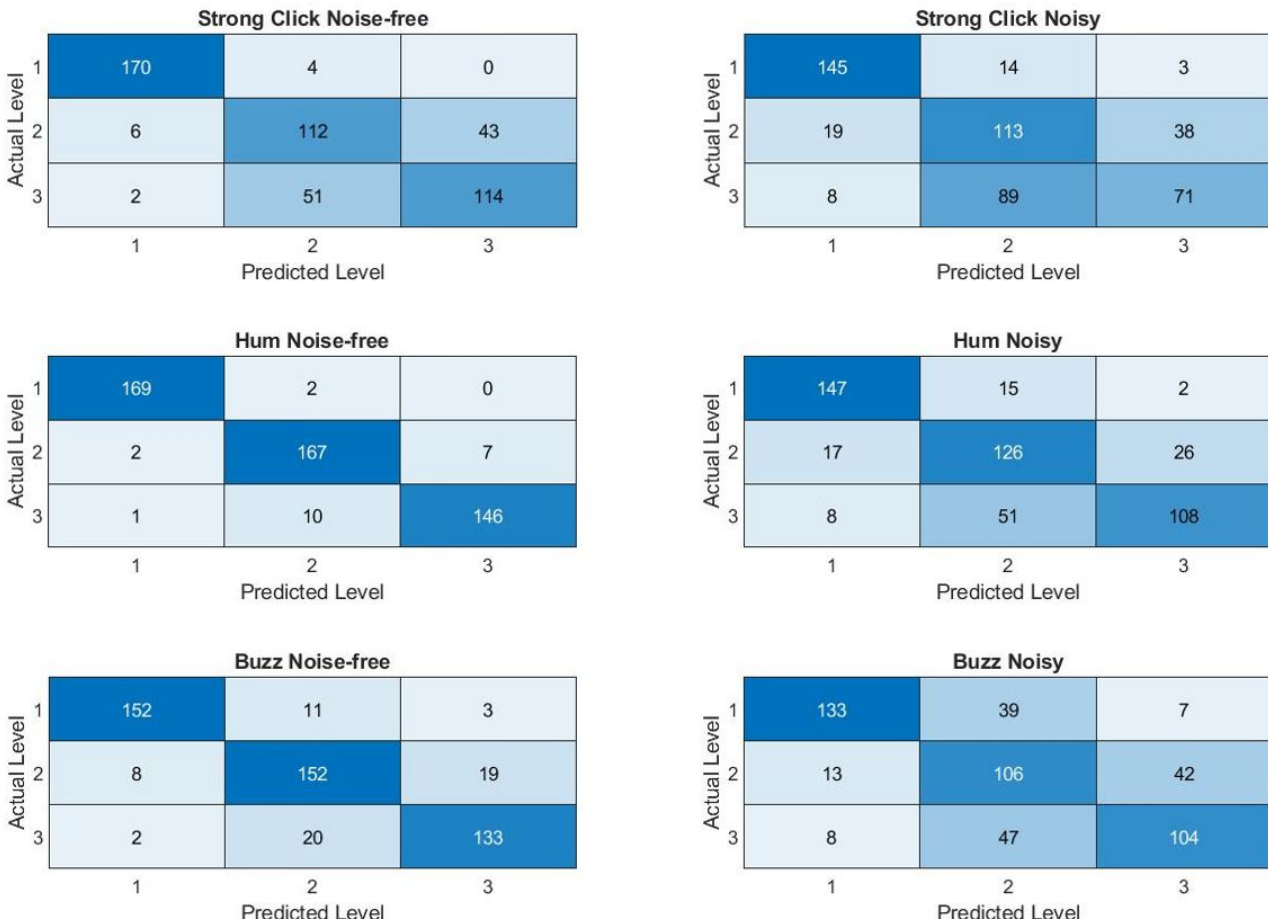


Figure 3.8: Confusion matrices for each stimulation waveform using amplitude modality, in both noise-free and noisy experimental conditions.

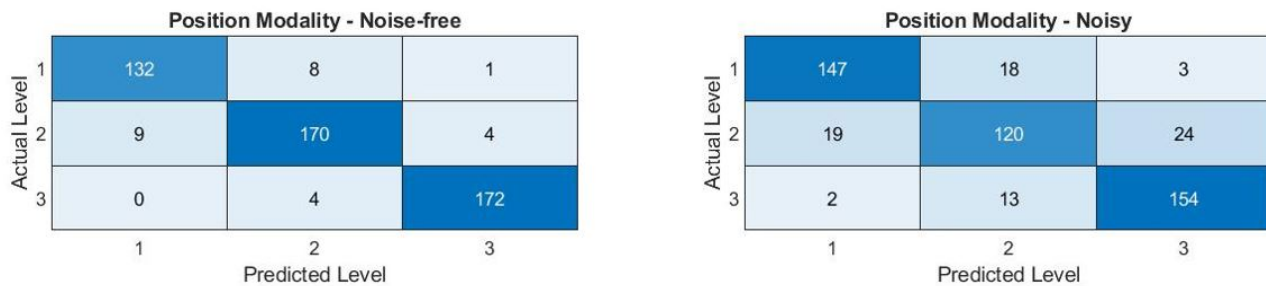


Figure 3.9: Confusion matrices for position modality, in both noise-free and noisy experimental conditions.

More detailed information regarding the confusion matrices of both modalities, in both experimental conditions, is provided in Tables 6.6-6.7 in Appendix 6.10.1. The confusion matrices were considered as unbalanced, due to unequal sample sizes of each class. Thus, normalisation of confusion matrices was done to make sample size of each class equal to 1. Normalisation process is explained in Appendix 6.10.2.

Three performance metrics [62] per stimulation level, namely F-score, per-class accuracy and specificity (Appendix 6.10.3), were calculated for the two best (in terms of classification accuracy) methods in noisy conditions, which are the position-modality and amplitude-modality (Hum) methods, based on normalised confusion matrices. These metrics are illustrated in Table 3.2. The performance metrics for the other methods are shown in Appendix 6.10.4.

Table 3.2: Per-class accuracy, specificity and F-score of the two methods in noisy conditions.

Method	Amplitude-modality (Hum)			Position-modality		
	1	2	3	1	2	3
<b>Stimulation Level</b>	<b>1</b>	<b>2</b>	<b>3</b>	<b>1</b>	<b>2</b>	<b>3</b>
Specificity(%)	90.36	79.54	90.82	92.77	90.66	90.71
F-score(%)	87.67	69.60	71.36	87.35	76.68	87.77
Accuracy(%)	90.08	77.85	81.50	90.87	84.92	90.86

### 3.3 Discussion

The results obtained from amplitude-modality experiments (Figure 3.7), indicate that the Hum waveform outperforms Strong Click and Buzz waveforms in both noise-free and noisy experimental conditions. Although levels 2 and 3 of Hum waveform were perceived as weaker compared to same levels of Strong Click and Buzz waveforms, participants reported more distinct differences between the two levels for Hum waveform (explaining its higher classification accuracy in both conditions).

In noise-free conditions, amplitude-modality based stimulation using Hum waveform and position-modality based stimulation had similar performance (with only 0.8% higher mean accuracy for amplitude-modality). In noisy experimental conditions, however, the position-modality method outperforms the amplitude-modality method (using Hum), having 8.0% higher mean classification accuracy (84.2%). This phenomenon occurs since vibration levels 2 and 3 in amplitude-modality method were perceived as weaker and less distinct compared to levels 2 and 3 in position-modality method. Thus, under noisy conditions, the two Hum waveform levels were more frequently misclassified. This is evident from the lower per-class accuracy and F-score of levels 2 and 3 in amplitude-modality method (Hum) with respect to same levels of position-modality method (Table 3.2). The position modality, despite having a 0.32% lower F-score for Level 1 and 0.11% lower specificity for Level 3, achieved 5.74% higher average per-class accuracy, 3.81% higher mean specificity and 7.73% higher average F-score than amplitude-modality method (Hum).

During this project, amplitude and position modalities were evaluated on only 5 individuals (due to unavailability of participants during COVID-19 lockdown) based on artificially generated stimulation signals from one area of foot. Therefore, future iterations would involve (1) larger sample sizes of participants, (2) simultaneous stimulation patterns from the three foot areas and (3) stimulation patterns on other upper-body locations (wrist, forearm or chest), to test effect of location on sensory feedback perception.

# Chapter 4

## Conclusion

Through thorough design considerations and testing, an in-sole FPS system has been successfully designed, that detects plantar pressure distributions, with RSS error 3.4478% and resolution 4.7998kPa, for body's CoP-shift computation. The extracted CoP-shift signals can be used as additional non-bioelectrical information to enhance performance of the sEMG-based MLP model in the lower-limb exoskeleton motion controller, for joint angle prediction.

Gait information, captured by plantar pressure distributions, can be also used as input sensory signals to the proposed HF system, to introduce close-loop control of exoskeleton. Initial results of HF system suggest that the position-modality stimulation method, under realistic (noisy) conditions outperforms all amplitude-modality methods, and yields overall classification accuracy of  $84.2 \pm 6.7454\%$ .

The combination of the two systems, with HF system operated under position-modality, is hypothesised to improve performance of exoskeleton motion control for the Cybathlon Competition. However, the assembly of FPS system was halted by the COVID-19 pandemic; thus, the two systems could not be tested under synchronous operation. Additionally, the unforeseen lab closure, postponed all planned experiments involving the exoskeleton, for assessment of controller's performance.

For future iterations of this study, the performance of the proposed feedback platform in combination with sEMG-based control algorithm can be evaluated, using kinematic data of joint angles from a motion capture system. This will allow identification of errors in exoskeleton motion, detection of incorrect motion patterns and abrupt changes in actuator angles. Moreover, the kinematic data obtained from the three systems combined, can be compared to data obtained using solely the sEMG sensors, to quantify any improvements in the overall performance.

# Chapter 5

## Bibliography

- [1] World Health Organisation (2013) *Spinal cord injury*. Available online: <https://www.who.int/news-room/fact-sheets/detail/spinal-cord-injury>
- [2] Yan, T. et al. (2015) *Review of assistive strategies in powered lower-limb orthoses and exoskeletons*, Robotics and Autonomous Systems. Elsevier B.V., 64, pp. 120–136. doi: 10.1016/j.robot.2014.09.032.
- [3] Sanz-Merodio D., Cestari M., Arevalo J.C. , Carrillo X., GarciaE. (2014) *Generation and control of adaptive gaits in lower-limb exoskeletons for motion assistance*,Adv. Robot. 28 329–338.
- [4] Veneman J.F. et al (2007) *Design and evaluation of the lopes exoskeleton robot for interactive gait rehabilitation* IEEE Trans. Neural Syst. Rehabil. Eng. 15 379–386.
- [5] Ryan J. Farris (2012) *Preliminary Evaluation of a Powered Lower Limb Orthosis to Aid Walking in Paraplegic Individuals*, IEEE Trans Neural Syst Rehabil Eng. 2011 December,19(6): 652–659. doi:10.1109/TNSRE. 2011.2163083.
- [6] Kagirov I.K. et al . (2019). *Lower Limbs Exoskeleton Control System Based on Intelligent Human-Machine Interface*. doi:10.1007/978-3-030-32258-8-54.
- [7] Suzuki, K. et al. (2012) *Intention-based walking support for paraplegia patients with Robot Suit HAL*, 1864.
- [8] Strausser, K. A. and Kazerooni, H. (2011) *The development and testing of a human machine interface for a mobile medical exoskeleton*, 2011 IEEE/RSJ International Conference on Intelligent Robots and Systems. IEEE, pp. 4911–4916. doi: 10.1109/IROS.2011.6095025.
- [9] Xu, F. et al. (2017) *Adaptive Stair-Ascending and Stair-Descending Strategies for Powered Lower Limb Exoskeleton*.
- [10] Al-quraishi, M. S. et al. (no date) *EEG-Based Control for Upper and Lower Limb Exoskeletons and Prostheses : A Systematic Review*, pp. 1–27. doi: 10.3390/s18103342.
- [11] Fleischer, C. and Wege, A. (2006) *Application of EMG signals for controlling exoskeleton robots*, pp. 314–319. doi: 10.1515/BMT.2006.063.
- [12] Kawamoto, H. et al. (2010) *Voluntary Motion Support Control of Robot Suit HAL Triggered by Bioelectrical Signal for Hemiplegia*, 2010 Annual International Conference of the IEEE Engineering in Medicine and Biology. IEEE, pp. 462–466. doi: 10.1109/IEMBS.2010.5626191.
- [13] Sczesny-kaiser, M. et al. (2015) *HAL exoskeleton training improves walking parameters and normalizes cortical excitability in primary somatosensory cortex in spinal cord injury patients*,

- Journal of NeuroEngineering and Rehabilitation. Journal of NeuroEngineering and Rehabilitation, pp. 1–11. doi: 10.1186/s12984-015-0058-9.
- [14] Jansen, O. et al. (2017) *Functional Outcome of Neurologic-Controlled HAL-Exoskeletal Neuromechanical Rehabilitation in Chronic Spinal Cord Injury : A Pilot With One Year Treatment and Variable Treatment Frequency*, 7(8), pp. 735–743. doi: 10.1177/2192568217713754
- [15] Technaid (2020) *Robotic Exoskeleton Exo-H3*.  
Website: <https://www.technaid.com/products/robotic-exoskeleton-exo-exoesqueleto-h3/>.
- [16] ETH Zurich (2019) *Race Task Description Cybathlon 2020 races*. Available online: <https://cybathlon.ethz.ch/races-and-disciplines/powered-exoskeleton-race.html>
- [17] Anders C. et al (2007) *Trunk muscle activation patterns during walking at different speeds*, Journal of Electromyography and Kinesiology 17.2 , pp. 245–252.
- [18] Pergolini A. (2019) *CYBATHLON 2020 Powered Exoskeleton Race*, Master's Thesis in Biomedical Engineering, Politecnico di Torino, Turin. Italy.
- [19] Hsu, W. et al. (no date) *The Design and Application of Simplified Insole-Based Prototypes with Plantar Pressure Measurement for Fast Screening of Flat-Foot*. doi: 10.3390/s18113617.
- [20] Salpavaara T. et al (2009) *Wireless Insole Sensor System for Plantar Force Measurements during Sport Events* Proceedings of IMEKO XIX World Congress on Fundamental and Applied Metrology, Lisbon, Portugal, 6–11 September 2009; pp. 2118–2123.
- [21] Rodgers, M. (1988) *Dynamic biomechanics of the normal foot and ankle during walking and running* Phys. Ther. 1988, 68, 1822–1830.
- [22] Lou, C. et al. (no date) *Dynamic Balance Measurement and Quantitative Assessment Using Wearable Plantar-Pressure Insoles in a Pose-Sensed Virtual Environment*. doi: 10.3390/s18124193.]
- [23] Wada, C. and Sugimura, Y. (2010) *Development of a rehabilitation support system with a shoe-type measurement device for walking*, Proceedings of SICE Annual Conference 2010. IEEE, pp. 2534–2537.
- [24] Low, J. H., Khin, P. M. and Yeow, C. H. (2015) *A Pressure - Redistributing Insole using Soft Sensors and Actuators*, 2015 IEEE International Conference on Robotics and Automation (ICRA). IEEE, pp. 2926–2930. doi: 10.1109/ICRA.2015.7139599.
- [25] Suprapto, S. S. et al. (2017) *Low-Cost Pressure Sensor Matrix Using Velostat*, IEEE, (November), pp. 6–7.
- [26] Hamid, A. et al. (2012) *Force Sensor Detection and Performance Evaluation of New Active System Ankle Foot Orthosis*, 41(Iris), pp. 510–515. doi: 10.1016/j.proeng.2012.07.205.
- [27] Zhang, Z. and Poslad, S. (2014) *Improved Use of Foot Force Sensors and Mobile Phone GPS for Mobility Activity Recognition*, IEEE, 14(12), pp. 4340–4347.
- [28] Varoto, R. et al. (2017) *A Low Cost Wireless System to Monitor Plantar Pressure using Insole Sensor: Feasibility Approach*, (Biostec), pp. 207–214. doi: 10.5220/0006246402070214.
- [29] Blaya, J. A. (2003) *Force-Controllable Ankle Foot Orthosis ( AFO ) to Assist Drop Foot Gait*.
- [30] Shu, L. et al (2009) *In-shoe plantar pressure measurement and analysis system based on fabric pressure sensing array*,IEEE Trans. Inf. Technol. Biomed. 14, 767–775.

- [31] G. C. Trachtenberg (2012) *Enhanced Foot Function and Gait Analysis Using the 3Box Approach with F-Scan*, Tekscan, Inc., Foot Pressure measurement in a Clinical setting, pp.6-7.
- [32] Hadi, A. et al. (2012) *Foot Plantar Pressure Measurement System: A Review*, pp. 9884–9912. doi: 10.3390/s120709884.
- [33] Urry S. (1999) *Plantar pressure-measurement sensors*. Measurement Science and Technology 10(1), R16-32. doi: 10.1088/0957-0233/10/1/017.
- [34] TE Connectivity Sensors (2019) *Compression Load Cell*, FX29 Datasheet, DOC Control Number: 05142019. Available online: <https://www.te.com/usa-en/product-CAT-FSE0006.html>
- [35] Atmel (2015) *8-bit AVR Microcontroller with 32K Bytes In-System Programmable Flash*, ATmega328P Datasheet, 7810D-AVR-01/15. Available online: [http://ww1.microchip.com/downloads/en/DeviceDoc/Atmel-7810-Automotive-Microcontrollers-ATmega328P\\_Datasheet.pdf](http://ww1.microchip.com/downloads/en/DeviceDoc/Atmel-7810-Automotive-Microcontrollers-ATmega328P_Datasheet.pdf)
- [36] Giovanelli, D. and Farella, E. (2016) *Force Sensing Resistor and Evaluation of Technology for Wearable Body Force Sensing Resistor and Evaluation of Technology for Wearable Body Pressure Sensing*, (February). doi: 10.1155/2016/9391850.
- [37] Hopkins, M., Vaidyanathan, R. and McGregor, A. H. (2020) *Examination of the Performance Characteristics of Velostat as an In-Socket Pressure Sensor*, IEEE, pp. 1–9. doi: 10.1109/JSEN.2020.2978431.
- [38] Tekscan Inc (2018), *FlexiForce Standard Model A201*. Available online: <https://www.tekscan.com/resources/product/flexiforce-a201-datasheet>.
- [39] Bamberg, S. J. M. et al. (2008) *Gait Analysis Using a Shoe-Integrated Wireless Sensor System*, 12(4), pp. 413–423.
- [40] Mecmesin (no date) *MultiTest-i Technical Datasheet*. Datasheet ref:431-343-09. Available from: <https://www.mecmesin.com/>
- [41] International Electrotechnical Commission (2008) *Process measurement and control devices – General methods and procedures for evaluating performance – Part 2: Tests under reference conditions*, pg.8-13, IEC 61298-2.
- [42] Novel GmbH (no date) *emed: Pressure distribution under the foot*. Available online: <https://www.novel.de/products/emed/>
- [43] Tekscan (no date) *F-Scan System*. Available online: <https://www.tekscan.com/products-solutions/systems/f-scan-system>
- [44] Smooth-On (no date) *SORTA-Clear™ Series Addition Cure Silicone Rubber Compounds*. Available online: [https://www.smooth-on.com/tb/files/SORTA\\_CLEAR\\_SERIES\\_TB.pdf](https://www.smooth-on.com/tb/files/SORTA_CLEAR_SERIES_TB.pdf)
- [45] Sarikhani, A. et al. (2016) *Studying Maximum Plantar Stress per Insole Design Using Foot CT-Scan Images of Hyperelastic Soft Tissues*.
- [46] Urry S. (1999) *Plantar pressure-measurement sensors*. Measurement Science and Technology 10(1), R16-32. doi: 10.1088/0957-0233/10/1/017
- [47] Fan, R. E. et al. (2008) *A Haptic Feedback System for Lower-Limb Prostheses*, 16(3), pp. 270–277.

- [48] Muijzer-witteveen, H., Guerra, F. and Sluiter, V. (2016) *Pneumatic Feedback for Wearable Lower Limb Exoskeletons Further Explored*, 1, pp. 90–98. doi: 10.1007/978-3-319-42321-0.
- [49] P. Marayong, I.-H. Khoo, K. Nguyen, N. Bharti, B. Ruhe, D. Craig, et al (2014) *Vibrotactile device for rehabilitative training of persons with lower-limb amputation*, Healthcare Innovation Conference (HIC), IEEE, pp. 157-160.
- [50] K. A. Kaczmarek, J. G. Webster, P. Bach-y-Rita, and W. J. Tompkins (1991) *Electrotactile and vibrotactile displays for sensory substitution systems*, IEEE Trans. Biomed. Eng., vol. 38, pp. 1–16.
- [51] Fan, R. E. et al. (2009) *Pilot testing of a haptic feedback rehabilitation system on a lower-limb amputee*, 2009 ICME International Conference on Complex Medical Engineering. IEEE, pp. 1–4. doi: 10.1109/ICCME.2009.4906637.
- [52] Sie, A. and Rombokas, E. (2017) *A Lower Limb Prosthesis Haptic Feedback System for Stair Descent*, pp. 1–2.
- [53] Crea, S. et al. (2015) *Providing Time-Discrete Gait Information by Wearable Feedback Apparatus for Lower-Limb Amputees : Usability and Functional Validation*, IEEE Transactions on Neural Systems and Rehabilitation Engineering. IEEE, 23(2), pp. 250–257. doi: 10.1109/TNSRE.2014.2365548.
- [54] Husman, M. A. B. et al. (2016) *A Wearable Skin Stretch Haptic Feedback Device : Towards Improving Balance Control in Lower Limb Amputees*, 2016 38th Annual International Conference of the IEEE Engineering in Medicine and Biology Society (EMBC). IEEE, pp. 2120–2123. doi: 10.1109/EMBC.2016.7591147.
- [55] Wafai, L. et al. (2015) *Identification of Foot Pathologies Based on Plantar Pressure Asymmetry*, 3, pp. 20392–20408. doi: 10.3390/s150820392.
- [56] Adafruit (2011) *Vibrating Mini Motor Disk*.  
Available online: <https://www.adafruit.com/product/1201#technical-details>
- [57] Stark, B., Carlstedt, T., Hallin, R. G. & Risling, M. (1998) *Distribution of human pacinian corpuscles in the hand*, Journal of Hand Surgery, 23 (3), 370-372. Available from: [http://dx.doi.org/10.1016/S0266-7681\(98\)80060-0](http://dx.doi.org/10.1016/S0266-7681(98)80060-0).
- [58] Lumen (2013) *Sensory Systems - Somatosensation*, Boundless Biology, accessed on 28/05/2020, URL:<https://courses.lumenlearning.com/boundless-biology/chapter/somatosensation/>
- [59] Texas Instruments (2012) *DRV2605 Haptic Driver for ERM and LRA With Built-In Library and Smart-Loop Architecture*, SLOS825C, p.p. 54. Available online: <https://cdn-shop.adafruit.com/datasheets/DRV2605.pdf>
- [60] Alva, S (2018) *Sensory Feedback in Upper Limb Prosthetics*.
- [61] Walter Boron & Emile Boulpaep (2016) *Somatic Sensory Receptors, Proprioception, and Pain*, Chapter 15, Medical Physiology, 3rd Edition, Elsevier.
- [62] Ali, M. et al. (2017) *An Accurate CT Saturation Classification Using a Deep Learning Approach Based on Unsupervised Feature Extraction and Supervised Fine-Tuning Strategy*, (Dc). doi: 10.3390/en10111830.
- [63] Ryoon, T., Jong, N. and Sik, M. (1999) *Quantification of the path of center of pressure (COP) using an F-scan in-shoe transducer*, 10, pp. 248–254.

- [64] Macrae, C. S. et al. (2016) *Do rocker-sole shoes influence postural stability in chronic low back pain? A randomised trial*, Appendix 2 - Centre of pressure calculations, pp.1-2. doi:10.1136/bmjsbm-2016-000170.
- [65] Watanabe, T. et al. (2011) *A Preliminary Test of Measurement of Joint Angles and Stride Length with Wireless Inertial Sensors for Wearable Gait Evaluation System*, doi: 10.1155/2011/975193.
- [66] Ashcroft (2015) *How accurate is your accuracy statement?*, Accuracy White Paper, 1.800.328.8258. Available online: <https://assets.tequipment.net/assets/1/7/Ashcroft-Accuracy-Whitepaper.pdf>
- [67] Mitchell S. Cottrell (2011) *ME240 Resources-Calibration*, Missouri University of Science and Technology. Available online: [web.mst.edu/~cottrell/ME240/Resources/Calibration/](http://web.mst.edu/~cottrell/ME240/Resources/Calibration/)
- [68] AE Sensors (2016) *Understanding Linearity*, 05. Available online: <https://aesensors.nl/assets/uploads/2016/05/Understanding-Linearity.pdf>
- [69] Precision Microdrives (2020) *Which haptic effects should you use?*, Accessed on 3 June 2020. Available online: <https://www.precisionmicrodrives.com/content/which-haptic-effects-should-you-use/>
- [70] Simske, S. (2019) *Chapter 4 - Meta-analytic design patterns*, in Simske, S. B. T.-M.-A. (ed.) Morgan Kaufmann, pp. 147–185. doi: <https://doi.org/10.1016/B978-0-12-814623-1.00004-6>.

# Chapter 6

## Appendices

### 6.1 Center of Pressure Calculations

The x- and y-coordinates of the CoP for left and right foot at each time instant  $t$ ,  $(\text{CoP}_{l,x}(t), \text{CoP}_{l,y}(t))$  and  $(\text{CoP}_{r,x}(t), \text{CoP}_{r,y}(t))$  respectively, are computed using Equations 6.1 and 6.2 and the total pressure value of each foot,  $p_{l,tot}(t)$  and  $p_{r,tot}(t)$ , using Equation 6.3, similar to the method followed by Ryoon T. et al [63]:

- $\text{CoP}_{l,x}(t) = \frac{\sum_{n=1}^N x_{l,n} p_{l,n}(t)}{\sum_{n=1}^N p_{l,n}(t)}$  and  $\text{CoP}_{l,y}(t) = \frac{\sum_{n=1}^N y_{l,n} p_{l,n}(t)}{\sum_{n=1}^N p_{l,n}(t)}$  (6.1)

- $\text{CoP}_{r,x}(t) = \frac{\sum_{n=1}^N x_{r,n} p_{r,n}(t)}{\sum_{n=1}^N p_{r,n}(t)}$  and  $\text{CoP}_{r,y}(t) = \frac{\sum_{n=1}^N y_{r,n} p_{r,n}(t)}{\sum_{n=1}^N p_{r,n}(t)}$  (6.2)

- $p_{l,tot}(t) = \sum_{n=1}^N p_{l,n}(t)$  and  $p_{r,tot}(t) = \sum_{n=1}^N p_{r,n}(t)$  (6.3)

where  $N$  is the total number of force sensors attached to the foot sole or shoe insole (which is the same for both feet),  $(x_{l,n}, y_{l,n})$  and  $(x_{r,n}, y_{r,n})$  are the x- and y-coordinates of the  $n^{th}$  sensor on left and right feet respectively,  $p_{l,n}(t)$  and  $p_{r,n}(t)$  are the pressure amplitudes at the location of the  $n^{th}$  sensor on left and right foot at time point  $t$ . All CoP calculations and sensor coordinates are considered with the respect to the origin  $(0,0)$  located at the posterior edge of the foot's calcaneal (heel) fat pad. Additionally the positive x-axis is considered in the anteroposterior direction and positive y-axis in the mediolateral direction. The CoP locations of each foot can be then combined in a form of a weighted summation to find the location of the CoP of the whole body  $(\text{CoP}_x(t), \text{CoP}_y(t))$ . To achieve this, a common fixed coordinate system between the two feet is required. For this reason, x- and y-coordinates of the CoP of each foot are considered with respect to the origin of the left foot, thus this requires translation of x and y components coordinates of CoP of right foot by instantaneous step length  $d_{step}(t)$  and stride width  $d_{width}(t)$ . According to [64] the coordinates of CoP of the whole body, denoted by  $(\text{CoP}_x(t), \text{CoP}_y(t))$ , can then be computed by Equations 6.4 and 6.5:

$$\text{CoP}_x(t) = \text{CoP}_{l,x}(t) \frac{p_{l,tot}(t)}{p_{l,tot}(t) + p_{r,tot}(t)} + (\text{CoP}_{r,x}(t) + d_{step}(t)) \frac{p_{r,tot}(t)}{p_{l,tot}(t) + p_{r,tot}(t)} \quad (6.4)$$

$$\text{CoP}_y(t) = \text{CoP}_{l,y}(t) \frac{p_{l,tot}(t)}{p_{l,tot}(t) + p_{r,tot}(t)} + (\text{CoP}_{r,y}(t) + d_{width}(t)) \frac{p_{r,tot}(t)}{p_{l,tot}(t) + p_{r,tot}(t)} \quad (6.5)$$

The computations described by Equations 6.1-6.3 are being performed by the responsible Arduino on each foot, and obtained values are then transmitted to the Central Microcontroller (Raspberry Pi) located in the upper body.

Within the Central Microcontroller, the CoP of the whole body is calculated using Equations 6.4 and 6.5. The instantaneous step length  $d_{step}$  can be computed from the model joint angles stored in the Central Microcontroller from the MLP. This step requires additional knowledge of

pilot's lower-limb segment lengths. Since the lower-limb exoskeleton used in this project has only two degrees of freedom for hip and knee joint, allowing rotation only in the sagittal and frontal plane, it is assumed that the stride width  $d_{width}$  remains constant with time with negligible time-variations due to freely-rotating ankle joint. Alternatively, both quantities can be measured through attachment of inertial sensors on pilot's shoes, as proposed by Watanabe, T. et al [65].

## 6.2 Alignment and resampling steps for FPS system

The raw data obtained from Force Tester and Arduino before performing any pre-processing method are shown in Figure 6.1.

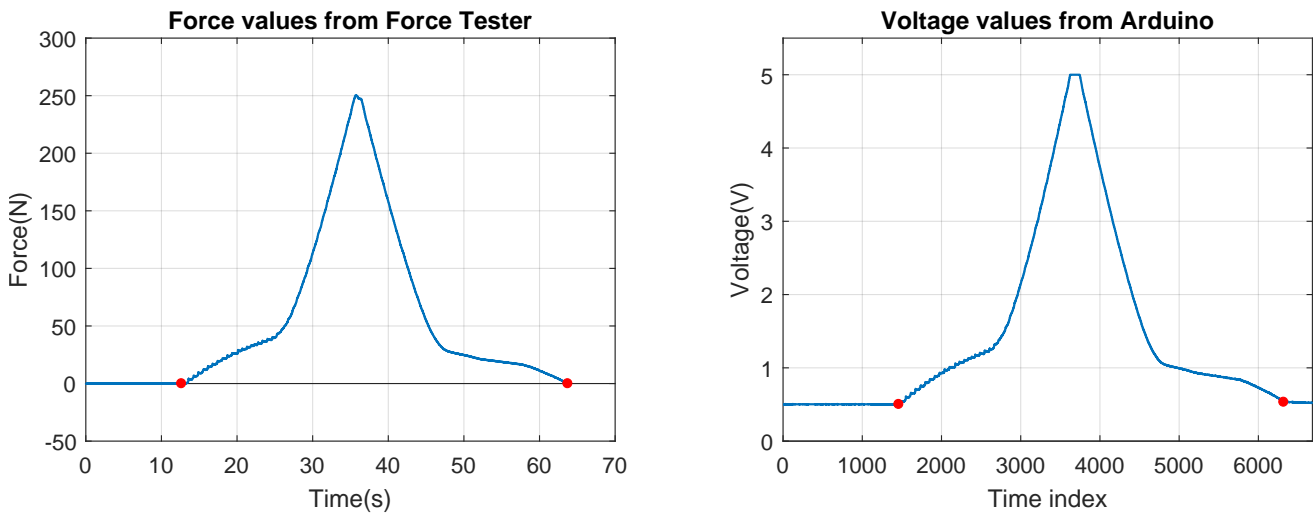


Figure 6.1: Original Force and Voltage data obtained (prior to alignment and resampling steps).

In order to plot the force values against voltage values, the force data must be down-sampled to ensure that both data have the same length. This is due to the higher sampling rate of MultiTest 5-xt software (1kHz). This was done using the built-in MATLAB function `resample()`, which applies an anti-aliasing FIR filter on force values prior to down-sampling. The down-sampling step was implemented using the following MATLAB code:

```

1 P=length(Force);
2 Q=length(Voltage);
3 Force_resampled = resample(Force,Q,P);
```

After resampling is performed, the plot of Force vs Voltage shown in Figure 6.2 is obtained. However, the results on this plot (showing for example high hysteresis) are misleading due to misalignment of data, i.e. onset of force increasing above 0N does not synchronously to the onset of voltage increasing above 0.5V.

To counteract this effect, the datasets must first be aligned and then force data must be re-sampled, using the method specified above.

The alignment of the two datasets was done automatically, by identifying algorithmically the two locations at which both force and voltage values start to increase above or decrease towards their baseline values. For the case of force values, the baseline value varies between 0-0.1485N with random deviations above and below this range due to noise. Therefore, the start location of force signal is the sample index at which three consecutive force values are above baseline. For the case of end location of force signal, the implemented algorithm finds the sample index at which force values decrease back to baseline value. The same procedure is also implemented for voltage signal, which has baseline value of 0.499-0.503V. The locations of start and end points of each dataset, acting as points of reference for alignment, are shown graphically as red markers in Figure 6.1.

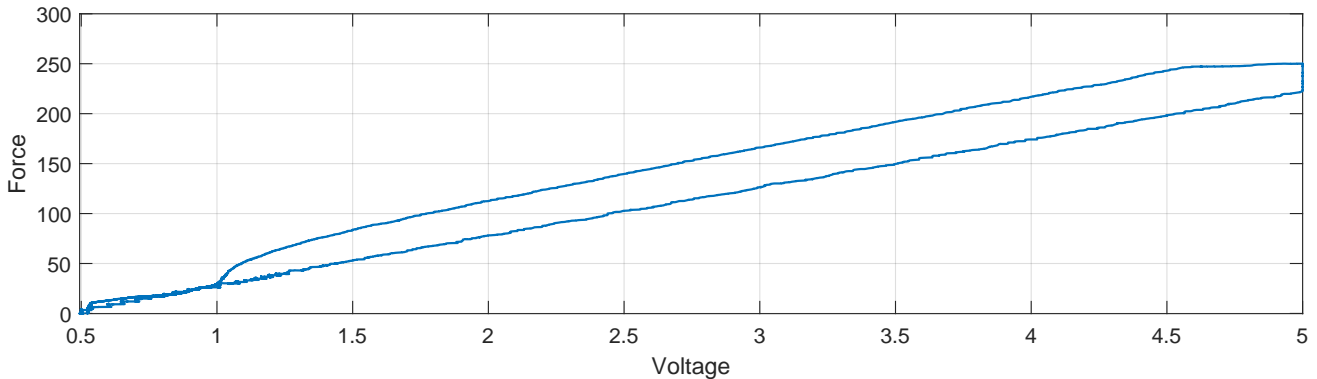


Figure 6.2: Plot of Force vs Voltage obtained after resampling was done on force data, but prior to alignment.

Once the desired points are identified, the two data sets are truncated such that any data before starting point and any data after end point is neglected.

Alternatively, the alignment procedure can be done by first re-scaling and then computing the cross-correlation of the two datasets.

In order to allow for visualisation of the results after the alignment and re-sampling step, i.e. by plotting time-evolution of resampled Force and Voltage values on the same plot, the voltage readings must first be re-scaled by  $\text{Voltage}_{\text{re-scaled}} = (\text{Voltage} - 0.5) \times 50$ .

The time evolution of force and voltage signals before and after alignment and resampling process are shown in Figure 6.3. Finally, the true Force vs Voltage plot is shown in Figure 6.4.

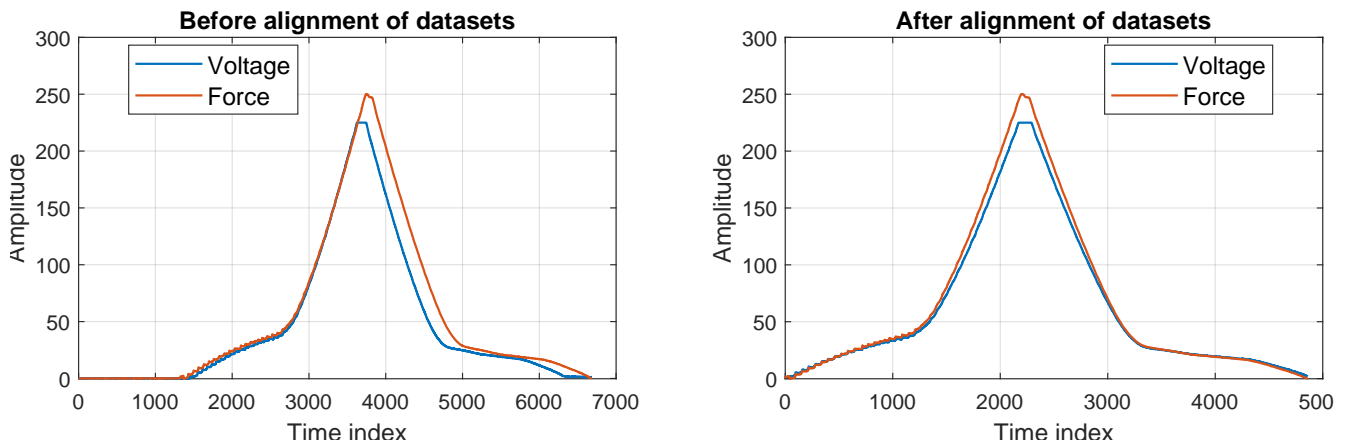


Figure 6.3: Force and Voltage signals (Left) before and after (Right) alignment and resampling procedure.

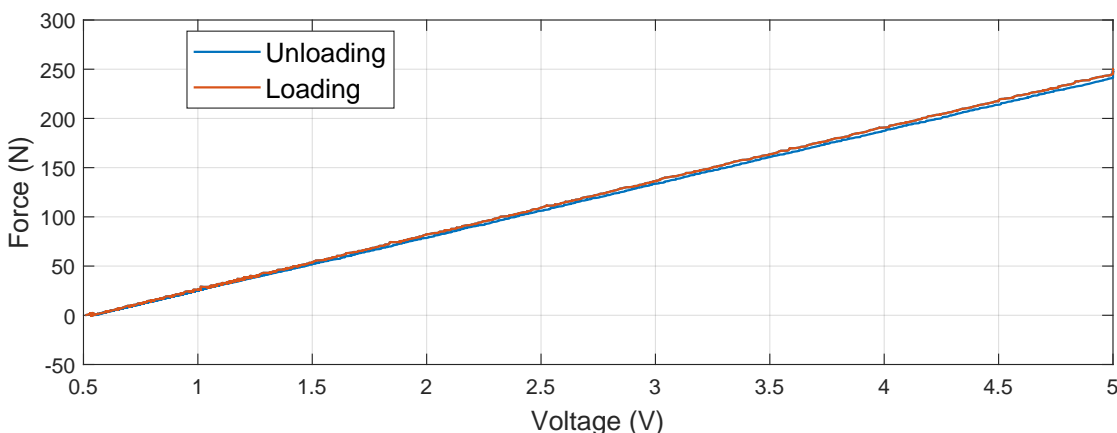


Figure 6.4: Force vs Voltage plot after alignment and resampling procedure.

## 6.3 Sensor Properties calculations

According to IEC 61298-2 [41], measurements of accuracy must include Hysteresis, Non-linearity and Non-repeatability errors. As explained in [66], in order to combine these three accuracy components into a single total accuracy measure, the Root of the Sum Squared (RSS) method is used, which is a very common method used by manufacturers. This method gives a metric to quantify the total error of system, where the three accuracy components are summed according to Equation 6.6.

$$\text{RSS } (\%) = \sqrt{(\text{Hysteresis})^2 + (\text{Non-linearity})^2 + (\text{Non-repeatability})^2} \quad (6.6)$$

All error values described in this section are expressed as a percentage of the sensor's full scale range. In other words, the absolute error values are divided by the difference between sensor's maximum output and minimum output.

### • Hysteresis Calculation

As seen by the Force-Voltage plot in Figure 6.4, the system behaves almost perfectly linearly with small non-linearity effects. This allows us to utilise the simplified method followed by Cottrell M.S [67]. The first step in the hysteresis calculation requires computation of the location of the mid-point of Force-Voltage Curve  $X_m$ , shown graphically in Figure 6.5.

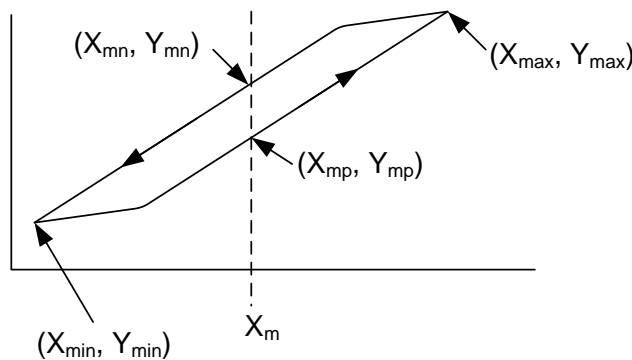


Figure 6.5: Simplified case for hysteresis calculation for almost perfectly linear systems, obtained from [67]. In this plot  $X$  corresponds to Voltage and  $Y$  corresponds to Force.

Following the notation used by Cottrell, the Voltage is denoted by  $X$  and Force by  $X$ . In the plot of Figure 6.5,  $(X_{min}, Y_{min})$  and  $(X_{max}, Y_{max})$  denote the minimum/maximum voltage and Force values respectively,  $X_{mp} = X_{mn} = X_m$  denote the mid-point voltage value, and  $Y_{mn}, Y_{mp}$  denote the force values at  $X_m$  in the top part and in the bottom part of plot respectively. The location of the mid-point along the voltage axis can be obtained using Equation 6.7.

$$X_m = \left( \frac{X_{max} - X_{min}}{2} \right) + X_{min} \quad (6.7)$$

Once the mid-point voltage value  $X_m$  is computed, the corresponding force values  $Y_{mn}$  and  $Y_{mp}$  are obtained, to be used in the calculation of hysteresis given by Equation 6.8.

$$\text{Hysteresis } (\%) = \left| \frac{(Y_{mn} - Y_{mp})}{(Y_{max} - Y_{min})} \right| \times 100\% \quad (6.8)$$

### • Non-linearity Error Calculation

The absolute Non-linearity Error, expressed as a percentage of full-scale sensor range, is sometimes referred to as linearity error. In order to quantify this error, the Best Fit Straight Line (BFSL) method was implemented, similar to the method followed by [68]. The first step of this method is the construction of a Least Squares Best Fit line through the loading curve of

the sensor. This can be obtained using the `polyfit()` MATLAB function, where the order of polynomial is equal to 1.

After the BFSL is constructed, the location of the maximum deviation of any point from this line ( $V_d$ ) is determined. The corresponding actual force value at this location is denoted by  $F_d$ , the corresponding force value on the BFSL is denoted by  $\bar{F}_d$ , the maximum force value as  $F_{max}$  and minimum force value as  $F_{min}$ . Using this notation, the absolute non-linearity error can be obtained using Equation 6.9.

$$\text{Non-linearity (\%)} = \left| \frac{(F_d - \bar{F}_d)}{(F_{max} - F_{min})} \right| \times 100\% \quad (6.9)$$

#### • Non-repeatability Calculation

The Non-Repeatability error is defined as the maximum difference in sensor output when the same force is applied, over different trials. To quantify this error, the loading curve is considered and the Voltage value at which the maximum difference between two trials occurs is determined. At this location, the corresponding force values ( $F_{d,i}$ ) are obtained and used in Equation 6.10.

$$\text{Non-repeatability (\%)} = \left| \frac{\max |F_{d,i} - F_{d,j}|}{(F_{max} - F_{min})} \right| \times 100\% , \text{ with } i, j \in [1, \dots, N] \text{ for } i \neq j. \quad (6.10)$$

where  $N$  is the number of experimental trials considered.

## 6.4 Silicone Mould Preparation details

The material used for silicone mould was SOR TA-Clear™ 40. This material is the product of a substrate, referred to as Part A, and a catalyst referred to as Part B. Table 6.1 shows the properties of material related to mould preparation process.

Table 6.1: Specification of SOR TA-Clear™ 40 [44].

Cure Time (hrs)	Specific Gravity (g/cm³)	Mix Ratio (by weight)	Pot Life (min)
16 hrs	1.08	100A:10B	60

#### • Protocol followed

1. Part A and B are pre-mixed thoroughly.
2. Part A and Part B are weighed using a gram scale in the ratio 100A:10B. Weight of Part A is determined based on volume required in application of interest.
3. The two Parts are dispensed in a mixing container (such as a paper or plastic cup) and mixed well for about 2-3 minutes, ensuring that material on container sides or bottom are scraped off. The dispensed material must fill about 1/3 of mixing container due to volume expansion of material occurring in Step 4.
4. Mixture within the mixing container is then degassed using a vacuum pump for 10 minutes at 29 inHg (98.205 kPa).
5. The mixture is then poured into the plastic container in a single spot where moulding will take place, with a flow as uniform as possible to minimise bubble formation.
6. The mixture within the plastic container is then degassed for additional 40 minutes at 29 inHg (98.205 kPa). Steps 4-6 are performed with minimum delay due to pot life of material being 60 minutes.
7. After vacuum degassing process is completed, the material is allowed to cure for at least 16 hours at room temperature (23°C).

- **Embedding single sensor in silicone mould**

The dimensions of the plastic container used in this process are: Height = 2.3cm, Length = 13.6cm, Width = 7.9cm (Area = 107.4400cm<sup>2</sup>). As Since the total height of insole is 1.35cm, then total volume of silicone rubber required is 145.044cm<sup>3</sup>. Since material has density of 1.08g/cm<sup>3</sup>, total mass of Part A needed is 156.65g and total mass of Part B is 15.67g (10:1 ratio). In the calculations that follow, the volume of Part B was assumed negligible. In other words, although 1.08g/cm<sup>3</sup> is the resulting density value of mixture, due to small amounts of catalyst (Part B) required, it was assumed that 1.08g/cm<sup>3</sup> is also the density of substrate.

The proportions (weights) of Part A and Part B required for each layer of mould are shown in Table 6.2.

Table 6.2: Proportions of Part A and Part B required for embedment of single sensor in silicone mould.

Layer	Height (cm)	Volume (cm <sup>3</sup> )	Part A mass (g)	Part B mass (g)
1	0.4	42.976	46.41	4.64
2	0.55	59.092	63.82	6.38
3	0.4	42.976	46.41	4.64

Despite the calculations being done for three layers of mould, the resulting product was only composed of two layers. After Layer 2 was created, the total height of insole was measured using a Vernier caliper to be 14mm, with Layer 1 height being 4.4mm and Layer 2 height being 8mm (2.5mm above sensor). For this reason, the creation of Layer 3 was omitted. The underestimated height of Layer 2 in the calculations was probably due to the fact that volume of cables (reinforced with mouldable glue Sugru), volume of sensors (equal to 1.68cm<sup>3</sup> corresponding to a height of 0.156mm) and volume of moulding pins/glue were omitted in calculations. Additionally, the material has probably expanded during degassing process or catalyst action. Furthermore, the plastic container was assumed to be perfectly rectangular, although area of base was smaller than area of top and its edges were not perfectly right-angle edges. Another possible reason of this miscalculation was the assumption that the volume of catalyst (Part B) was assumed negligible compared to volume of Part A. On the other hand, the calculations must allow some degree of underestimation due to material remaining on the sides of mixture container.

- **Silicone mould for insoles of both feet**

The plastic container to be used (was not implemented) for moulding of insoles of both legs, has dimensions: Height = 5.5cm, Length = 30.3cm, Width = 21.6cm. To create a mould of height 1.35cm, the volume of silicone rubber required for each insole is 441.774cm<sup>3</sup>. This means that for each sole 477.12g of Part A and 47.71g of Part B are required.

## 6.5 Polynomial Regression models for each trial

- Linear Models

Linear Regression						
			Trial			
Sensor Index	Sensor Serial Number	Measurement	1	2	3	4
1	198090043	F vs V model	F=54.8277V-31.5998	F = 53.1478V-27.9177	F = 53.0924V-27.3333	F= 53.1422V-27.976
		RMSE	4.6559	1.0886	1.3450	1.8620
		R <sup>2</sup>	0.9947	0.9997	0.9996	0.9992
2	198090051	F vs V model	F=53.5201V-27.7356	F=53.5242V-28.1103	F=53.4454V-27.4629	F=53.4309V-27.2814
		RMSE	0.2919	1.3747	0.9234	0.3049
		R <sup>2</sup>	0.999979	0.9995	0.9998	0.99998
3	198090064	F vs V model	F=53.0435V-28.0106	F=52.8982V-27.1384	F=52.8967V-26.9843	F=52.8807V-26.9879
		RMSE	1.0681	0.5398	0.2501	1.1650
		R <sup>2</sup>	0.9997	0.9999	0.999985	0.9997
4	198090077	F vs V model	F=53.2926V-28.5532	F=53.2581V-28.1102	F = 53.2588V-27.3274	F=53.2284V-27.0153
		RMSE	1.1049	0.8739	0.4307	1.7923
		R <sup>2</sup>	0.9997	0.9998	0.999955	0.9992
5	198090017	F vs V model	F=53.1284V-26.8879	F = 53.1213V -27.0116	F = 53.1195V -26.9469	F = 53.1317V -26.9661
		RMSE	0.5689	0.2073	0.2520	0.3278
		R <sup>2</sup>	0.9999	0.999988	0.999982	0.9999699
6	198090087	F vs V model	F=53.5473V -27.6802	F = 53.5217V -27.3891	F = 53.5391V -27.64	F = 53.5064V -27.4579
		RMSE	0.2357	0.4149	0.2739	0.5934
		R <sup>2</sup>	0.999985	0.999952	0.999979	0.999904

Figure 6.6: Linear Regression models for the six sensors of one foot insole in each trial, before being embedded in silicone mould. For each sensor, the corresponding model equation,  $R^2$  and RMSE values are shown.

- Quadratic Models

Quadratic Regression						
			Trial			
Sensor Index	Sensor	Measurement	1	2	3	4
1	198090043	F vs V model	F=0.40549V <sup>2</sup> + 56.6435V- 33.0211	F=0.0117V <sup>2</sup> + 53.0951V- 27.8771	F=-0.0763V <sup>2</sup> + 53.4305V- 27.5877	F=0.091475V <sup>2</sup> + 52.7354V- 27.6691
		RMSE	4.6323	1.0885	1.3418	1.8587
		R <sup>2</sup>	0.9947	0.9997	0.9996	0.9992
2	198090051	F vs V model	F=0.0028292V <sup>2</sup> + 53.5075V- 27.7259	F=0.076837V <sup>2</sup> + 53.18V- 27.8426	F=-0.12618V <sup>2</sup> + 54.0068V- 27.895	F=-0.11972V <sup>2</sup> + 53.9619V- 27.6782
		RMSE	0.2919	1.3717	0.9112	0.2679
		R <sup>2</sup>	0.9999789	0.9995	0.9998	0.999983
3	198090064	F vs V model	F=0.24426V <sup>2</sup> +51.9463V- 27.1441	F=0.040453V <sup>2</sup> +52.7178V- 27.0019	F=0.0011304V <sup>2</sup> +52.8916V- 26.9804	F=-0.003333V <sup>2</sup> +52.8954V- 26.9989
		RMSE	1.0291	0.5375	0.2501	1.1650
		R <sup>2</sup>	0.9997	0.9999	0.999985	0.9997
4	198090077	F vs V model	F=0.20018V <sup>2</sup> +52.3899V- 27.8662	F=0.085821V <sup>2</sup> +52.8762V- 27.8268	F=-0.18594V <sup>2</sup> +54.0801V- 27.937	F=-0.36444V <sup>2</sup> +54.8354V- 28.1995
		RMSE	1.0773	0.8676	0.3684	1.7386
		R <sup>2</sup>	0.9997	0.9998	0.999967	0.9993
5	198090017	F vs V model	F=-0.097363V <sup>2</sup> +53.5672V- 27.2368	F=-0.055291V <sup>2</sup> +53.3729V- 27.2167	F=-0.067473V <sup>2</sup> +53.4285V- 27.2003	F=-0.066522V <sup>2</sup> +53.4359V- 27.2152
		RMSE	0.5595	0.1988	0.2414	0.3200
		R <sup>2</sup>	0.9999	0.999988	0.999984	0.999971
6	198090087	F vs V model	F=-0.094037V <sup>2</sup> +53.979V- 28.0388	F=-0.17944V <sup>2</sup> +54.3402V- 28.0605	F=-0.11126V <sup>2</sup> +54.0468V- 28.0558	F=-0.16017V <sup>2</sup> +54.2384V- 28.0576
		RMSE	0.2137	0.3693	0.2470	0.5680
		R <sup>2</sup>	0.999987	0.9999618	0.999983	0.999912

Figure 6.7: Quadratic Regression models for the six sensors of one foot insole in each trial, before being embedded in silicone mould. For each sensor, the corresponding model equation,  $R^2$  and RMSE values are shown.

- Cubic Models

Cubic Regression						
			Trial			
Sensor Index	Sensor	Measurement	1	2	3	4
1	198090043	F vs V model	$F=-1.0847V^3 + 7.1097V^2 + 42.0116V - 25.6804$	$F=-0.07878V^3 + 0.56175V^2 + 52.0221V - 27.3501$	$F=-0.053998V^3 + 0.29686V^2 + 52.7115V - 27.2413$	$F=-0.15038V^3 + 1.1334V^2 + 50.7232V - 26.6985$
		RMSE	4.4704	1.0847	1.3404	1.8507
		R <sup>2</sup>	0.9951	0.9997	0.9996	0.9992
2	198090051	F vs V model	$F=-0.069526V^3 + 0.48441V^2 + 52.5721V - 27.2642$	$F=-0.12413V^3 + 0.93888V^2 + 51.5V - 27.0111$	$F=-0.024621V^3 + 0.043916V^2 + 53.6777V - 27.7342$	$F=-0.024802V^3 + 0.051181V^2 + 53.6346V - 27.5226$
		RMSE	0.2816	1.3647	0.9107	0.2664
		R <sup>2</sup>	0.99998	0.9995	0.9998	0.999983
3	198090064	F vs V model	$F=-0.15453V^3 + 1.3207V^2 + 49.836V - 26.08$	$F=-0.06808V^3 + 0.51274V^2 + 51.8043V - 26.5599$	$F=-0.048438V^3 + 0.33824V^2 + 52.2393V - 26.6672$	$F=-0.064602V^3 + 0.44288V^2 + 52.0382V - 26.5901$
		RMSE	1.0147	0.5317	0.2435	1.1626
		R <sup>2</sup>	0.9997	0.9999	0.999986	0.9997
4	198090077	F vs V model	$F=-0.19057V^3 + 1.5304V^2 + 49.8035V - 26.6072$	$F=-0.14609V^3 + 1.0975V^2 + 50.9311V - 26.900$	$F=-0.021038V^3 - 0.040824V^2 + 53.8016V - 27.804$	$F=0.018161V^3 - 0.48958V^2 + 55.0751V - 28.3137$
		RMSE	1.0544	0.8511	0.3677	1.7385
		R <sup>2</sup>	0.9997	0.9998	0.999967	0.9993
5	198090017	F vs V model	$F=-0.0031804V^3 - 0.075127V^2 + 53.5231V - 27.2135$	$F=0.010523V^3 - 0.12952V^2 + 53.5223V - 27.2973$	$F=0.0123V^3 - 0.15459V^2 + 53.6046V - 27.2956$	$F=0.0080737V^3 - 0.12368V^2 + 53.5514V - 27.2777$
		RMSE	0.5595	0.1985	0.2411	0.3199
		R <sup>2</sup>	0.999910	0.999989	0.999984	0.999971
6	198090087	F vs V model	$F=-0.024122V^3 + 0.077091V^2 + 53.6311V - 27.8482$	$F=-0.017819V^3 - 0.053705V^2 + 54.0866V - 27.923$	$F=-0.015623V^3 - 0.00088363V^2 + 53.8239V - 27.9353$	$F=-0.02168V^3 - 0.0068059V^2 + 53.9285V - 27.8901$
		RMSE	0.2124	0.3689	0.2464	0.5676
		R <sup>2</sup>	0.999988	0.999962	0.999983	0.999912

Figure 6.8: Cubic Regression models for the six sensors of one foot insole in each trial, before being embedded in silicone mould. For each sensor, the corresponding model equation,  $R^2$  and RMSE values are shown.

## 6.6 Average Polynomial Regression models

- Average Linear Models

The average linear models for each of the six sensors of a foot insole, prior to embedment in silicone mould are shown in Figure 6.9. To obtain these models, the regression coefficients were averaged across the four trials. The model obtained in the  $k^{\text{th}}$  trial is given by Equation 6.11.

$$F_k = a_{0,k} + a_{1,k}V \quad (6.11)$$

Therefore, to obtain the average Force value ( $\bar{F}$ ) across trials:

$$\bar{F} = \frac{1}{4} \sum_{k=1}^4 F_k = \frac{1}{4} \sum_{k=1}^4 \sum_{i=0}^1 a_{i,k} V^i = \sum_{i=0}^1 V^i \frac{1}{4} \sum_{k=1}^4 a_{i,k} = \sum_{i=0}^1 \bar{a}_i V^i = \bar{a}_0 + \bar{a}_1 V \quad (6.12)$$

where  $\bar{a}_i$  denotes the average  $i^{\text{th}}$  coefficient.

Linear Model						
			Trial			
Sensor Index	Sensor Serial Number	Measure	1	2	3	4
1	198090043	$R^2$	0.9941	0.9997	0.9994	0.9991
		RMSE	4.9161	1.1944	1.5456	1.9268
		General Equation	$F = 53.5525V - 28.7067$			
2	198090051	$R^2$	0.999978	0.9995	0.9998	0.999959
		RMSE	0.2960	1.4269	0.9320	0.4149
		General Equation	$F = 53.4801V - 27.6476$			
3	198090064	$R^2$	0.9996	0.9999	0.999972	0.9997
		RMSE	1.1937	0.5475	0.3447	1.1838
		General Equation	$F = 52.9298V - 27.2803$			
4	198090077	$R^2$	0.9996	0.9998	0.9999	0.9991
		RMSE	1.3303	0.9456	0.6036	1.9176
		General Equation	$F = 53.2595V - 27.7515$			
5	198090017	$R^2$	0.999906	0.999987	0.999982	0.9999699
		RMSE	0.5733	0.2174	0.2522	0.3279
		General Equation	$F = 53.1252V - 26.9531$			
6	198090087	$R^2$	0.999982	0.999946	0.999978	0.9999037
		RMSE	0.2584	0.4380	0.2853	0.5954
		General Equation	$F = 53.5286V - 27.5418$			

Figure 6.9: Average Linear Regression models for the six sensors of one foot insole, before being embedded in silicone mould. For each sensor, the corresponding model equation,  $R^2$  and RMSE values are shown.

- **Average Quadratic Models**

The average quadratic models for each of the six sensors of a foot insole, prior to embedding in silicone mould are shown in Figure 6.10. To obtain these models, the regression coefficients were averaged across the four trials. The model obtained in the  $k^{\text{th}}$  trial is given by Equation 6.13.

$$F_k = \sum_{i=0}^2 a_{i,k} V^i \quad (6.13)$$

Therefore, to obtain the average Force value ( $\bar{F}$ ) across trials:

$$\bar{F} = \frac{1}{4} \sum_{k=1}^4 F_k = \frac{1}{4} \sum_{k=1}^4 \sum_{i=0}^2 a_{i,k} V^i = \sum_{i=0}^2 V^i \frac{1}{4} \sum_{k=1}^4 a_{i,k} = \sum_{i=0}^2 \bar{a}_i V^i \quad (6.14)$$

where  $\bar{a}_i$  denotes the average  $i^{\text{th}}$  coefficient.

Quadratic Model						
Sensor Index	Sensor Serial Number	Measure	Trial			
			1	2	3	4
1	198090043	$R^2$	0.9941	0.9997	0.9994	0.9991
		RMSE	4.9070	1.2001	1.5478	1.9375
		General Equation	$F = -0.094654V^2 + 53.9761V - 29.0387$			
2	198090051	$R^2$	0.999978	0.9995	0.9998	0.999962
		RMSE	0.3010	1.4317	0.9250	0.4005
		General Equation	$F = -0.041558V^2 + 53.664V - 27.7854$			
3	198090064	$R^2$	0.9996	0.9999	0.999971	0.9997
		RMSE	1.1762	0.5453	0.3494	1.1857
		General Equation	$F = 0.070627V^2 + 52.6128V - 27.0313$			
4	198090077	$R^2$	0.9996	0.9998	0.9999	0.9991
		RMSE	1.3472	0.9570	0.5791	1.9014
		General Equation	$F = -0.0066096V^2 + 53.5454V - 27.9574$			
5	198090017	$R^2$	0.9999087	0.999987	0.9999838	0.999971
		RMSE	0.5649	0.2105	0.2416	0.3202
		General Equation	$F = -0.071662V^2 + 53.4511V - 27.2172$			
6	198090087	$R^2$	0.999984	0.999956	0.999981	0.9999115
		RMSE	0.2441	0.3976	0.2607	0.5709
		General Equation	$F = -0.13623V^2 + 54.1511V - 28.0532$			

Figure 6.10: Average Quadratic Regression models for the six sensors of one foot insole, before being embedded in silicone mould. For each sensor, the corresponding model equation,  $R^2$  and RMSE values are shown.

- Average Cubic Models

The average cubic models for each of the six sensors of a foot insole, prior to embedment in silicone mould are shown in Figure 6.11. To obtain these models, the regression coefficients were averaged across the four trials. The model obtained in the  $k^{\text{th}}$  trial is given by Equation 6.15.

$$F_k = \sum_{i=0}^3 a_{i,k} V^i \quad (6.15)$$

Therefore, to obtain the average Force value ( $\bar{F}$ ) across trials:

$$\bar{F} = \frac{1}{4} \sum_{k=1}^4 F_k = \frac{1}{4} \sum_{k=1}^4 \sum_{i=0}^3 a_{i,k} V^i = \sum_{i=0}^3 V^i \frac{1}{4} \sum_{k=1}^4 a_{i,k} = \sum_{i=0}^3 \bar{a}_i V^i \quad (6.16)$$

where  $\bar{a}_i$  denotes the average  $i^{\text{th}}$  coefficient.

Cubic Model						
Sensor Index	Sensor Serial Number	Measure	Trial			
			1	2	3	4
1	198090043	$R^2$	0.9943	0.9996	0.9994	0.9991
		RMSE	4.8232	1.2227	1.5594	1.9337
		General Equation	$F = -0.34197V^3 + 2.2754V^2 + 49.3671V - 26.7426$			
2	198090051	$R^2$	0.999979	0.9995	0.9998	0.999962
		RMSE	0.2909	1.4268	0.9255	0.3991
		General Equation	$F = -0.06077V^3 + 0.37959V^2 + 52.8461V - 27.383$			
3	198090064	$R^2$	0.9996	0.9999	0.999972	0.9997
		RMSE	1.1638	0.5393	0.3440	1.1827
		General Equation	$F = -0.08391V^3 + 0.65364V^2 + 51.4795V - 26.4743$			
4	198090077	$R^2$	0.9996	0.9998	0.9999	0.9991
		RMSE	1.3341	0.9451	0.5822	1.9050
		General Equation	$F = -0.084884V^3 + 0.52438V^2 + 52.4028V - 27.4062$			
5	198090017	$R^2$	0.9999	0.999987	0.999984	0.99997
		RMSE	0.5650	0.2103	0.2413	0.3201
		General Equation	$F = 0.006929V^3 - 0.12073V^2 + 53.5504V - 27.271$			
6	198090087	$R^2$	0.999984	0.999956	0.999981	0.999912
		RMSE	0.2428	0.3973	0.2603	0.5704
		General Equation	$F = -0.019811V^3 + 0.00392V^2 + 53.8675V - 27.8992$			

Figure 6.11: Average Cubic Regression models for the six sensors of one foot insole, before being embedded in silicone mould. For each sensor, the corresponding model equation,  $R^2$  and RMSE values are shown.

## 6.7 Silicone mould effects on Force-Voltage models

The average linear, quadratic and cubic models for a single sensor, before and after being embedded in silicone mould are compared in Table 6.3.

Table 6.3: Comparison of average models for single sensor pre- and post-embedding in silicone mould.

Average Linear Model		Before embedding in Silicone				After embedding in Silicone			
		Trial				Trial			
Sensor	Measure	1	2	3	4	1	2	3	4
198090064	R <sup>2</sup>	0.9996	0.9999	0.99997	0.9997	0.9986	0.9970	0.9989	0.9983
	RMSE	1.1937	0.5475	0.3447	1.1838	2.2822	3.3638	2.0830	2.5289
	General Equation	$F = 52.9298V - 27.2803$				$F = 148.1166V - 65.975$			
Average Quadratic Model		Before embedding in Silicone				After embedding in Silicone			
		Trial				Trial			
Sensor	Measure	1	2	3	4	1	2	3	4
198090064	R <sup>2</sup>	0.9996	0.9999	0.99971	0.9997	0.9988	0.9972	0.9990	0.9986
	RMSE	1.1762	0.5453	0.3494	1.1857	2.1458	3.2644	1.9815	2.3259
	General Equation	$F = 0.070627V^2 + 52.6128V - 27.0313$				$F = -5.2028V^2 + 159.4927V - 71.4732$			
Average Cubic Model		Before embedding in Silicone				After embedding in Silicone			
		Trial				Trial			
Sensor	Measure	1	2	3	4	1	2	3	4
198090064	R <sup>2</sup>	0.9996	0.9999	0.99997	0.9997	0.9989	0.9974	0.9990	0.9986
	RMSE	1.1638	0.5393	0.3440	1.1827	2.0561	3.1756	1.9413	2.2936
	General Equation	$F = -0.08391V^3 + 0.65364V^2 + 51.4795V - 26.4743$				$F = 12.2281V^3 - 45.0215V^2 + 199.0223V - 83.1479$			

## 6.8 Waveform Description for Amplitude Modality

The three waveforms (Strong Click, Hum and Buzz) and their corresponding amplitudes used in amplitude-modality method, that were selected from DRV2605 datasheet [59], are shown in Table 6.4. Note that Level 4 denotes the stimulation level at which amplitude of motor vibration is 0 (thus motor is OFF).

Table 6.4: Stimulation Waveforms and corresponding vibration amplitude levels used.

<b>Amplitude</b>	<b>Waveform</b>		
	<i>Strong Click</i>	<i>Hum</i>	<i>Buzz</i>
<b>Level 1 (%)</b>	100	100	100
<b>Level 2 (%)</b>	60	60	60
<b>Level 3 (%)</b>	30	20	40
<b>Level 4 (%)</b>	0	0	0

The different vibration waveforms produced by DRV2605 controller are illustrated in Figure 6.12, obtained from Precision Microdrives website [69]. The waveforms of interest in Figure 6.12 are the “Clicks” and “Buzzes”, where the latter also include the Hum waveform.

Strong Clicks are considered are short-duration (sharp) vibration effects, where the motor reaches its peak vibration in a very short time. In the case of Buzz waveform, a soft symmetrical (compared to ramps) vibration is produced whose peak value is usually sustained at the mid-point of waveform for short-time periods. The Hum waveform is very similar to Buzz waveform, but it is smoother in shape. All vibration waveforms can be thought of as delivering the same overall amount of mechanical energy (due to vibration), i.e. same area under amplitude vs time plots, however with different duration and peak amplitude values.

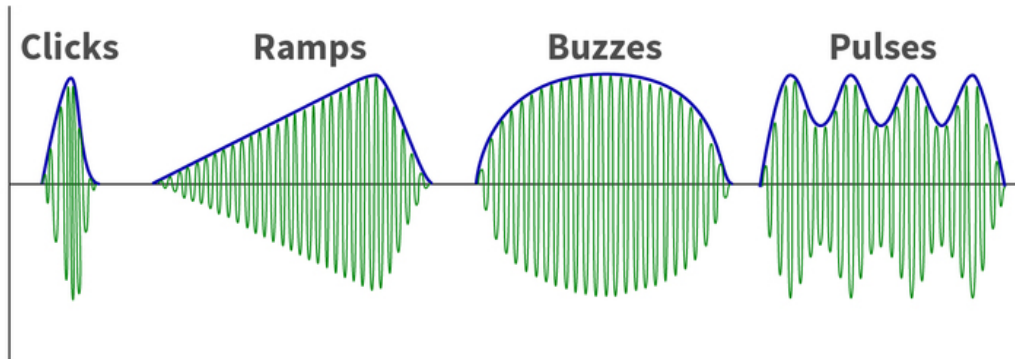


Figure 6.12: Different Forms of Vibration waveforms (how vibration amplitude changes over time). Figure obtained from [69].

The DRV2605 output voltage waveform can be analysed using an oscilloscope, or connecting the “+” pin of motor controller to an Arduino analogue pin and “-” pin to ground. The Arduino voltage readings can be stored on a computer using CoolTerm software, and then analysed in MATLAB to produce plots of voltage signal waveforms. Additionally, to visualise and analyse vibration waveforms of Ada1201 motors controlled by DRV2605 driver circuit, force sensors with high sensitivity (higher resolution than FX29 series sensors used in FPS system) can be used. This allows measurements of vibration frequencies and characterisation of vibration shape. To measure the amplitude of vibrations, a distance proximity sensor can be used, e.g. Infra-red sensors, can be used to measure displacement amplitudes of sensor during vibration.

## 6.9 Details on Position-Modality Circuit

According to [56], the rated input DC voltage for Adafruit 1201 motors is between 2-5V. The current draw at each input voltage level is shown in Table 6.5.

Table 6.5: Current draw of Ada1201 motors for maximum amplitude vibration at each voltage supply level.

Input Voltage	5V	4V	3V	2V
Current Draw	100mA	80mA	60mA	40mA

As specified by Adafruit website [56], the motor can be activated directly by the Arduino digital pins (without need for implementation of low-side MOSFET switch circuits). This can be done by connecting the blue cable of motor to the Arduino pin and red cable to ground. Therefore, by setting the digital pin to “HIGH” (5V) the motor will vibrate and when digital pin is set to “LOW” (0V), the motor stops vibrating. However, according to ATmega328P datasheet [35], the absolute maximum current for any single digital Input/Output pin is 40 mA. Therefore, this means that when digital output is set to 5V, the current draw of the motor will be around 40mA and the motor will not vibrate at maximum amplitude. In general, the higher the current draw, the higher the amplitude (strength) of motor vibration (increase in current, increases angular frequency of motor and in turn increases vibration magnitude; although above a critical angular frequency, vibration magnitude starts to decrease). What is more, resistors between 100 to 1000Ω can be connected in series between the Arduino digital pins and motors to reduce the current draw below 40mA, and hence reduce amplitude.

The problem with this circuit, however, is that it can only decrease vibration strength. By assuming a linear relationship between current draw and vibration amplitude, directly connecting the motors to digital pins set at 5V (40mA), is expected to produce (in the best-case) approximately 2.5 times lower vibration magnitude compared to the amplitude that would have been obtained at 100mA.

In order to increase the vibration amplitude, the low-side MOSFET switch method was considered where the Arduino digital pin only controls the Gate-to-Source ( $V_{GS}$ ) voltage of transistor. The transistors used, had  $V_{GS(th)}$  Gate Threshold Voltage between 2.0 and 4.0 V so that they can be controlled with logic level and also have a Drain-to-Source On-Resistance ( $R_{DS(on)}$ ) = 0.2Ω, thus ensuring low voltage drop (approximately 20mV) across MOSFET transistor. In this circuit (Figure 3.5), the Motor’s ground cable is connected to MOSFET’s Drain, Motor’s power cable was connected to 3.3V (or 5V) output pin of Arduino and the Source of MOSFET was connected to GND. According to [35], the 5V output pin can have 400mA current output when Arduino is powered on USB (due to USB interface) or 900mA when an external power adapter is used, that provides voltage >7V. The 3.3V output of Arduino can only supply at maximum 150mA (due to 3.3V regulator).

Considering the circuit used, where an array of three Ada1201 motors connected in parallel is being powered by the 3.3V Arduino pin, it means that each motor in the array receives approximately at maximum 50mA. If, however, the low-side MOSFET circuit was not used, but instead motors were powered directly from the Arduino digital pins, then each motor would receive at maximum 40mA. Therefore, low-side MOSFET switch allows higher magnitude vibrations (the higher the current the higher the amplitude). In the case that the motor array was powered by 5V pin of Arduino, then each motor would receive 100mA regardless if Arduino is powered through USB or external power supply. Additionally, by connecting a variable resistor in series with 5V pin and each motor, the motor vibration can be adjusted to lower amplitudes.

Considering the case where the pressure values from three foot sole areas are mapped into haptic vibration using the position-modality approach, then a total of 9 motors would be needed. By connecting each motor to Arduino digital pins, then each motor receives 40mA. By connecting these motors of the three arrays to 3.3V pin and low-side MOSFET switch topology

is used, each motor would receive only 16.67mA, thus directly controlling them by digital pins results in higher amplitude vibrations. Finally, in the case that each motor is connected to 5V pin of Arduino through the low-side MOSFET switch circuit, current draw by each motor is 55.56mA when Arduino is powered via USB and can increase up to 100mA when an external power supply (between 7V and 9V) is used.

## 6.10 Confusion Matrices

### 6.10.1 Analysis of Confusion Matrices from perceptual experiments

The confusion matrices obtain in both amplitude- and position-modality, in both noise-free and noisy experimental conditions, based experiments were further analysed, as shown in Tables 6.6 and 6.7. These indicate the number of occurrences of each stimulation level (out of 500 total stimulation levels), number of correct and incorrect classification. These were used to obtain mean accuracy in each experimental condition for both modalities and also the average over both experimental conditions was obtained.

Table 6.6: Further analysis of experimental results for amplitude modality.

	Amplitude Modality					
	Strong Click		Hum		Buzz	
	Noise-free	Noisy	Noise-free	Noisy	Noise-free	Noisy
<b>Total samples</b>	500	500	500	500	500	500
<b>Number of occurrences of each level (Level1,Level 2,Level 3)</b>	(174,161,165)	(162,170,168)	(171,172,157)	(164,169,167)	(166,179,155)	(179,161,160)
<b>Correct Classifications</b>	396	329	478	381	437	343
<b>Incorrect Classifications</b>	104	171	22	119	63	157
<b>Mean Accuracy (%)</b>	79.2	65.8	95.6	76.2	87.4	68.6
<b>Overall accuracy (%)</b>	72.20		86.35		78.00	

Table 6.7: Further analysis of experimental results for position modality.

	Position Modality	
	Noise-free	Noisy
<b>Total samples</b>	500	500
<b>Number of occurrences of each level (Level1,Level 2,Level 3)</b>	(141,183,176)	(168,163,169)
<b>Correct Classifications</b>	474	421
<b>Incorrect Classifications</b>	26	79
<b>Mean Accuracy (%)</b>	94.8	84.2
<b>Overall accuracy (%)</b>	89.4	

### 6.10.2 Normalisation of Confusion Matrices

Normalisation is required when the confusion matrices are unbalanced, i.e. the sample size of each class is not the same. In fact, during the haptic system perceptual tests, the number of occurrences for each stimulation level (class) were not the same.

Direct analysis of these unbalanced or skewed data will result in biased results. Thus to remove the effect of sample size on performance metrics for each method, the confusion matrices are first normalised [70]. This can be done by dividing each element of the confusion matrix by the sum of the elements in the corresponding row, i.e. by its sample size. This ensures that the sum of each row in the matrix is equal to 1. In other words, the normalisation process makes sample size of each class equal to 1.

The normalised confusion matrices for the amplitude-modality based method (for all stimulation waveforms) and position-modality based method, for both noise-free and noisy experimental conditions, shown in Figures 6.13 and 6.14 .

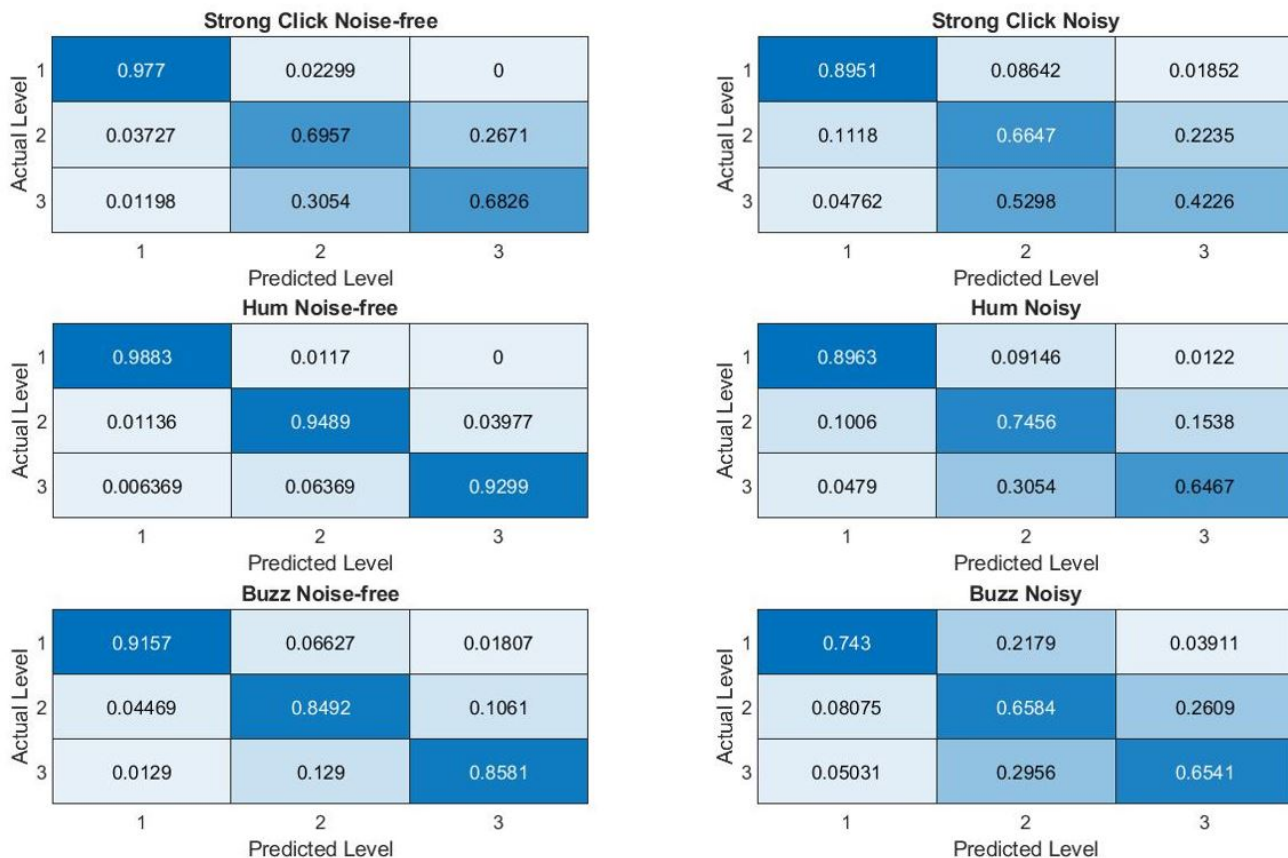


Figure 6.13: Normalised Confusion matrices for Amplitude-modality method, for all stimulation waveforms in both Noise-free and noisy conditions.

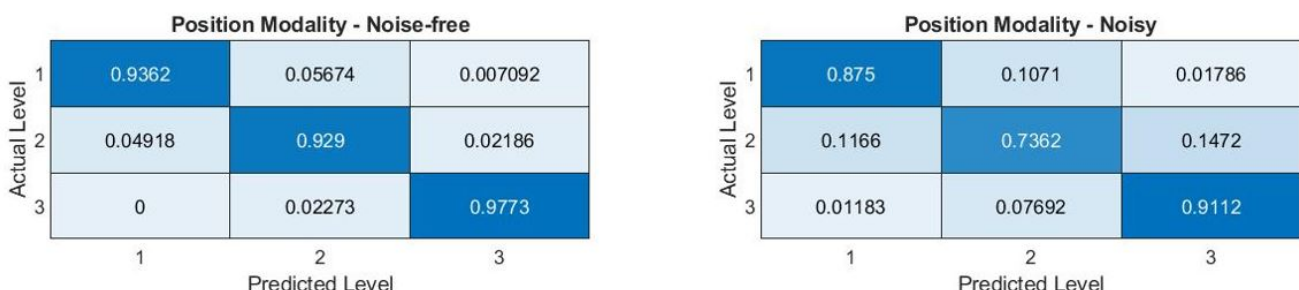


Figure 6.14: Normalised Confusion matrices for Position-modality method, in both Noise-free and noisy conditions.

### 6.10.3 Mathematical Definitions

Figure 6.15, obtained from [62], shows a general case of a confusion matrix for multi-class classification task, specifically for three classes.

Confusion Matrix	Predicted			False Negative (FN)	Recall
	Class 1	Class 2	Class 3		
Actual	Class 1	A	B	C	B + C
	Class 2	D	E	F	D + F
	Class 3	G	H	I	G + H
False Positive (FP)					Overall Accuracy = A + E + I / (Sum of red and green squares)
	D + G	B + H	C + F		
Precision	A / (A + D + G)	E / (B + E + H)	I / (C + F + I)		

True positives ■ True Negatives ■ Misclassified cases ■ False Positives ■ False Negatives.

Figure 6.15: Illustration of how different performance metrics for each class are computed. Image obtained from [62].

Different performance metrics can be obtained for each class using the confusion matrix obtained from the classification task. These metrics are based on the number of True Positives (TP), True Negatives (TN), False Positives (FP) and False Negatives (FN). FN and FP calculations for each class are illustrated in Figure 6.15. The number of TP of a class is equal to the value within the green box corresponding to that class, and number of TN is the sum of values of green boxes not belonging that class. For instance, TP for Class 1 is A, while TN for Class 1 is E+I.

The definitions of different metrics are summarised in Equations 6.17-6.21, based on definitions of TP, TN, FP and FN described before.

- Per-class Accuracy =  $\frac{TP + TN}{TP + TN + FP + FN}$  (6.17)

- Precision =  $\frac{TP}{TP + FP}$  (6.18)

- Sensitivity or Recall =  $\frac{TP}{TP + FN}$  (6.19)

- Specificity or Selectivity =  $\frac{TN}{FP + TN}$  (6.20)

- F-score =  $2 \frac{\text{Precision} \times \text{Recall}}{\text{Precision} + \text{Recall}} = \frac{2TP}{2TP + FP + FN}$  (6.21)

It should be mentioned that the F-score, defined by Equation 6.21, is equal to the harmonic mean of the precision and recall. The ideal F-score value is 1, in which case there is perfect precision and sensitivity.

### 6.10.4 Per-class Performance metrics of all methods

The following plots show the performance metrics of each class for all methods, apart from Noisy Position-modality based method, using normalised confusion matrices.

Performance Metric	Class		
	Level 1	Level 2	Level 3
<b>True Positives (TP) ratio</b>	0.977011	0.695652	0.682635
<b>True Negatives (TN) ratio</b>	1.378287	1.659646	1.672664
<b>False Positives (FP) ratio</b>	0.049243	0.328378	0.267081
<b>False Negatives (FN) ratio</b>	0.022989	0.304348	0.317365
<b>Per-class accuracy (%)</b>	97.02	78.82	80.12
<b>Precision (%)</b>	95.20	67.93	71.88
<b>Sensitivity (%)</b>	97.70	69.57	68.26
<b>Specificity (%)</b>	96.55	83.48	86.23
<b>F-score (%)</b>	96.44	68.74	70.02
<b>Average per-class Accuracy (%)</b>		85.32	

Figure 6.16: Performance metrics of each class for Amplitude-modality method, using Strong Click Waveform in Noise-free conditions.

Performance Metric	Class		
	Level 1	Level 2	Level 3
<b>True Positives (TP) ratio</b>	0.895062	0.664706	0.422619
<b>True Negatives (TN) ratio</b>	1.087325	1.317681	1.559768
<b>False Positives (FP) ratio</b>	0.159384	0.616182	0.242048
<b>False Negatives (FN) ratio</b>	0.104938	0.335294	0.577381
<b>Per-class accuracy (%)</b>	88.24	67.57	70.75
<b>Precision (%)</b>	84.88	51.89	63.58
<b>Sensitivity (%)</b>	89.51	66.47	42.26
<b>Specificity (%)</b>	87.22	68.14	86.57
<b>F-score (%)</b>	87.13	58.28	50.78
<b>Average per-class Accuracy (%)</b>		75.52	

Figure 6.17: Performance metrics of each class for Amplitude-modality method, using Strong Click Waveform in Noisy conditions.

Performance Metric	Class		
	Level 1	Level 2	Level 3
<b>True Positives (TP) ratio</b>	0.988304	0.948864	0.929936
<b>True Negatives (TN) ratio</b>	1.8788	1.91824	1.937168
<b>False Positives (FP) ratio</b>	0.017733	0.07539	0.039773
<b>False Negatives (FN) ratio</b>	0.011696	0.051136	0.070064
<b>Per-class accuracy (%)</b>	98.98	95.77	96.31
<b>Precision (%)</b>	98.24	92.64	95.90
<b>Sensitivity (%)</b>	98.83	94.89	92.99
<b>Specificity (%)</b>	99.06	96.22	97.99
<b>F-score (%)</b>	98.53	93.75	94.42
<b>Average per-class Accuracy (%)</b>		97.02	

Figure 6.18: Performance metrics of each class for Amplitude-modality method, using Hum Waveform in Noise-free conditions.

<b>Performance Metric</b>	<b>Class</b>		
	Level 1	Level 2	Level 3
<b>True Positives (TP) ratio</b>	0.896341	0.745562	0.646707
<b>True Negatives (TN) ratio</b>	1.392269	1.543048	1.641904
<b>False Positives (FP) ratio</b>	0.148496	0.396853	0.166041
<b>False Negatives (FN) ratio</b>	0.103659	0.254438	0.353293
<b>Per-class accuracy (%)</b>	90.08	77.85	81.50
<b>Precision (%)</b>	85.79	65.26	79.57
<b>Sensitivity (%)</b>	89.63	74.56	64.67
<b>Specificity (%)</b>	90.36	79.54	90.82
<b>F-score (%)</b>	87.67	69.60	71.35
<b>Average per-class Accuracy (%)</b>	83.14		

Figure 6.19: Performance metrics of each class for Amplitude-modality method, using Hum Waveform in Noisy conditions.

<b>Performance Metric</b>	<b>Class</b>		
	Level 1	Level 2	Level 3
<b>True Positives (TP) ratio</b>	0.915663	0.849162	0.858065
<b>True Negatives (TN) ratio</b>	1.707227	1.773727	1.764825
<b>False Positives (FP) ratio</b>	0.057596	0.195297	0.124218
<b>False Negatives (FN) ratio</b>	0.084337	0.150838	0.141935
<b>Per-class accuracy (%)</b>	94.87	88.34	90.79
<b>Precision (%)</b>	94.08	81.30	87.35
<b>Sensitivity (%)</b>	91.57	84.92	85.81
<b>Specificity (%)</b>	96.74	90.08	93.42
<b>F-score (%)</b>	92.81	83.07	86.57
<b>Average per-class Accuracy (%)</b>	91.33		

Figure 6.20: Performance metrics of each class for Amplitude-modality method, using Buzz Waveform in Noise-free conditions.

<b>Performance Metric</b>	<b>Class</b>		
	Level 1	Level 2	Level 3
<b>True Positives (TP) ratio</b>	0.743017	0.658385	0.654088
<b>True Negatives (TN) ratio</b>	1.312473	1.397105	1.401402
<b>False Positives (FP) ratio</b>	0.13106	0.513475	0.299976
<b>False Negatives (FN) ratio</b>	0.256983	0.341615	0.345912
<b>Per-class accuracy (%)</b>	84.12	70.62	76.09
<b>Precision (%)</b>	85.01	56.18	68.56
<b>Sensitivity (%)</b>	74.30	65.84	65.41
<b>Specificity (%)</b>	90.92	73.12	82.37
<b>F-score (%)</b>	79.29	60.63	66.95
<b>Average per-class Accuracy (%)</b>	76.94		

Figure 6.21: Performance metrics of each class for Amplitude-modality method, using Buzz Waveform in Noisy conditions.

<b>Performance Metric</b>	<b>Class</b>		
	Level 1	Level 2	Level 3
<b>True Positives (TP) ratio</b>	0.93617	0.928962	0.977273
<b>True Negatives (TN) ratio</b>	1.906234	1.913443	1.865132
<b>False Positives (FP) ratio</b>	0.04918	0.079465	0.02895
<b>False Negatives (FN) ratio</b>	0.06383	0.071038	0.022727
<b>Per-class accuracy (%)</b>	96.18	94.97	98.21
<b>Precision (%)</b>	95.01	92.12	97.12
<b>Sensitivity (%)</b>	93.62	92.90	97.73
<b>Specificity (%)</b>	97.48	96.01	98.47
<b>F-score (%)</b>	94.31	92.51	97.42
<b>Average per-class Accuracy (%)</b>	96.45		

Figure 6.22: Performance metrics of each class for Position-modality method in Noise-free conditions.

<b>Performance Metric</b>	<b>Class</b>		
	Level 1	Level 2	Level 3
<b>True Positives (TP)</b>	0.875	0.736196	0.911243
<b>True Negatives (TN)</b>	1.647439	1.786243	1.611196
<b>False Positives (FP)</b>	0.128399	0.184066	0.165096
<b>False Negatives (FN)</b>	0.125	0.263804	0.088757
<b>Per-class accuracy (%)</b>	90.87	84.92	90.86
<b>Precision (%)</b>	87.20	80.00	84.66
<b>Sensitivity (%)</b>	87.50	73.62	91.12
<b>Specificity (%)</b>	92.77	90.66	90.71
<b>F-score (%)</b>	87.35	76.68	87.77
<b>Average per-class Accuracy (%)</b>	88.88		

Figure 6.23: Performance metrics of each class for Position-modality method in Noisy conditions.